Pedagogic Null Tests of Dynamical Dark Energy Hints: Reconstructing ΛCDM with Consistent BAO, CMB, and SNe Mocks

Seokcheon Lee^{1,*}

¹Department of Physics, Institute of Basic Science, Sungkyunkwan University, Suwon 16419, Korea (Dated: November 24, 2025)

Hints of a dynamical dark-energy equation of state have appeared in several combined cosmological probes. However, such indications may instead arise from the intrinsic likelihood geometry of individual datasets, residual inter-probe tension, or restrictive priors. These factors can mimic evidence for dynamical dark energy. To clarify these issues, we perform a controlled null test. We use realistic mock BAO, CMB, and Type Ia supernova datasets generated from a common fiducial $\Lambda \mathrm{CDM}$ cosmology. These mocks include the DESI DR2 BAO covariance, the Planck 2018 distanceprior covariance, and the full Pantheon+ SH0ES supernova covariance. This setup isolates physical information from geometric or statistical effects in the CPL parametrization. We find that individual probes and most two-probe combinations show apparent deviations in the (ω_0, ω_a) plane. These could be mistaken for phantom crossing or evolving dark energy. Two-probe combinations including supernovae (BAO+SNe, CMB+SNe) recover values near $(\omega_0, \omega_a) = (-1, 0)$ but fail to reconstruct (Ω_{m0}, H_0) , because SNe do not determine the absolute distance scale. Combinations without SNe (BAO+CMB), as well as any single dataset, retain strong degeneracy directions. These produce significant shifts driven purely by likelihood geometry. These behaviors arise because BAO, CMB, and SNe each constrain only one principal direction in (ω_0, ω_a) space. Their degeneracy ridges are misaligned due to distinct redshift sensitivities. In contrast, the full BAO+CMB+SNe likelihood with proper covariance breaks all degeneracies simultaneously. It cleanly recovers the fiducial cosmology, including $(\omega_0, \omega_a) = (-1, 0)$ and (Ω_{m0}, H_0) . Our results provide a transparent benchmark for assessing future claims of $\omega(z) \neq -1$. They emphasize the need for complete multi-probe analyses with flexible H_0 and r_d priors.

CONTENTS

1. Introduction	2
II. Theoretical Framework: CPL, Pivot Formalism, Multi-Probe Geometry, and Bias Equation	2
A. CPL degeneracy and its geometric origin	3
B. Pivot equation of state and decorrelation	3
C. Bias equation under partial or inconsistent likelihoods	3
D. Geometric compensation in the CMB–BAO–SNe system	4
III. Mock Likelihoods: DESI-like BAO, Planck-like CMB, and Pantheon-like SNe	4
A. DESI-like BAO: D_M/r_d and D_H/r_d	5
B. Planck-like CMB distance priors	5
C. Pantheon-like Supernovae with full covariance	6
D. Combined likelihood and cross-probe consistency	6
IV. Multi-Probe Constraints from BAO, CMB, and SNe Mock Data	6
A. BAO-only Constraints	6
B. CMB-only Constraints	8
C. SNe-only Constraints	8
D. Joint BAO+CMB Constraints	10
E. Joint BAO+SNe Constraints	12
F. Joint CMB+SNe Constraints	13
G. Joint BAO+CMB+SNe Constraints	16
H. Comparative Constraints from All Probe Combinations	17

^{*} skylee@skku.edu

References 20

I. INTRODUCTION

Recent multi-probe analyses have reported apparent deviations from the cosmological-constant equation of state (EOS) (ω_0 , ω_a) = (-1,0), often interpreted as hints of dynamical dark energy (DDE) [1–5]. Whether such deviations signal new physics or instead reflect probe-specific sensitivities, residual systematics, or mismatched likelihood treatments remains actively debated [6–10]. In particular, Bayesian model comparisons reveal that the DESI DR2–Planck combination shows no preference for $\omega_0\omega_a$ CDM over Λ CDM, and that the mild preference for a time-varying EOS emerging when DES-Y5 supernovae (SNe) are added originates mainly from a $\sim 3\sigma$ DESI–DES-Y5 tension rather than a robust DDE signal [11, 12].

Several analyses have pointed out that such apparent deviations may, in part, reflect the structure of the likelihood itself rather than unambiguous signatures of DE evolution [13–18]. Different cosmological probes sample different redshift regimes: low-redshift SNe constrain the shape of $D_L(z)$ and therefore tightly anchor Ω_{m0} [19, 20]; intermediate-redshift baryon acoustic oscillation (BAO) constrain the comoving and Hubble distances $(D_M/r_d, D_H/r_d)$ and are more sensitive to combinations involving ω_a [21, 22]; and cosmic microwave background (CMB) distance priors probe a high-redshift weighted combination of the form $\Omega_{m0} + \kappa \omega_a$ with $\kappa \simeq 0.6$ –0.8 [23, 24]. Because each probe constrains only one effective direction in the (ω_0, ω_a) plane, their degeneracy directions are inherently misaligned [25–27]. Statistically, this misalignment leads to broad, elongated posteriors when only a subset of probes is used, and the posterior mean naturally shifts along the dominant degeneracy ridge [28, 29]. Mathematically, this behaviour reflects the structure of the distance integrals: low-redshift luminosity distances are dominated by Ω_{m0} , whereas intermediate-redshift BAO distances depend primarily on $\Omega_{m0} + \beta \omega_a$, and CMB distances are sensitive to a different high-redshift combination [21, 22, 25]. Thus, even perfect Λ CDM data can yield apparently non- Λ CDM constraints when analyzed with partial or compressed likelihoods [20, 29, 30].

The goal of this work is to provide a controlled and transparent demonstration of this phenomenon. We therefore generate DESI-like BAO [1, 2], Planck-like CMB distance priors [31–33], and Pantheon-like SNe datasets [6] from a single fiducial Λ CDM cosmology, using the actual DESI DR2 BAO covariance matrix, Planck 2018 distance-prior covariance, and the full Pantheon+ SH0ES supernova covariance. We then analyze each probe individually, each pairwise combination, and the full BAO+CMB+SNe likelihood. By keeping the underlying cosmology fixed and employing realistic observational covariances, this multi-probe framework isolates the physical, statistical, and mathematical origins of the inferred posterior structure, allowing us to determine when spurious signatures of DDE arise and under what conditions the fiducial cosmology is cleanly recovered.

Our null test reveals a consistent pattern: individual probes and most two-probe combinations generically produce displaced (ω_0 , ω_a) posteriors that resemble phantom crossing, late-time transitions, or mild early-DE behaviour. Because both the mock generation and the MCMC inference employ the full DESI DR2 BAO, Planck 2018 distance-prior, and Pantheon+ SH0ES covariance matrices, these displaced posteriors arise despite using fully realistic observational uncertainties. Only the full BAO+CMB+SNe combination—where the low-, intermediate-, and high-redshift constraints are simultaneously enforced—breaks all degeneracies and recovers the fiducial (ω_0 , ω_a) = (-1,0) model with high precision. This provides a direct demonstration that apparent DDE signals found in partial likelihoods may arise entirely from likelihood geometry rather than from new physics, underscoring the need for consistent multi-probe analyses in future high-precision surveys.

The structure of this paper is as follows. Section II reviews the CPL parametrization, the pivot formalism, and the geometric origin of degeneracy directions. Section III describes the DESI-like BAO, Planck-like CMB, and Pantheon-like SNe mock likelihoods. Section IV presents the constraints from all single-probe, pairwise, and fully joint analyses. Section V summarizes the implications of our null test for interpreting future DDE claims.

II. THEORETICAL FRAMEWORK: CPL, PIVOT FORMALISM, MULTI-PROBE GEOMETRY, AND BIAS EQUATION

In this section, we establish the theoretical tools required for our multi-probe mock analysis. We first review the geometric origin of the (ω_0, ω_a) degeneracy in the Chevallier–Polarski–Linder (CPL) parametrization and explain how different cosmological probes trace distinct directions in this parameter space. We then introduce the pivot formalism, which identifies the best-constrained combination of the DE EOS and provides a decorrelated representation of DDE constraints. Finally, we present the general Fisher-based bias equation that quantifies how incomplete or mismatched

likelihood combinations can generate spurious shifts in (ω_0, ω_a) , motivating the controlled multi-probe null tests performed in this work.

A. CPL degeneracy and its geometric origin

The CPL parametrization [34, 35],

$$\omega(z) = \omega_0 + \omega_a \frac{z}{1+z},\tag{1}$$

remains the standard two-parameter expansion for describing DDE. Its utility lies in the approximate linearity of $\omega(z)$ at low redshift and in its geometric interpretation. Different cosmological probes sample distinct redshift ranges and therefore respond to different linear combinations of (ω_0, ω_a) . In the background expansion,

$$H^{2}(z)/H_{0}^{2} \equiv E^{2}(z) = \Omega_{r0}(1+z)^{4} + \Omega_{m0}(1+z)^{3} + (1-\Omega_{m0}-\Omega_{r0})(1+z)^{3(1+\omega_{0}+\omega_{a})} \exp\left[-3\omega_{a}\frac{z}{1+z}\right], \quad (2)$$

where the paramaters Ω_{m0} and Ω_{r0} denote the present-day matter and radiation density fractions, respectively. Small, compensating variations in the CPL parameters that satisfy $\delta\omega_a \simeq -A\,\delta\omega_0$ leave the DE contribution in E(z) nearly unchanged across a broad redshift range, thereby producing the well-known degeneracy ridge in the (ω_0, ω_a) plane. The coefficient A depends on the redshift coverage of the probe: BAO constrains the intermediate-z distance scale, CMB fixes the high-redshift acoustic scale, and SNe measure the low-redshift luminosity distance

$$D_L(z) = (1+z)\frac{c}{H_0} \int_0^z \frac{dz'}{E(z')}.$$
 (3)

The combination of these three observables therefore probes complementary projections of the CPL plane.

B. Pivot equation of state and decorrelation

A convenient reparameterization is provided by the pivot EOS [36–38]

$$\omega_p = \omega_0 + (1 - a_p)\omega_a, \qquad a_p = 1 + \frac{\text{Cov}(\omega_0, \, \omega_a)}{\text{Var}(\omega_a)},$$
(4)

for which $\mathrm{Cov}(\omega_p,\,\omega_a)=0$. Geometrically, ω_p isolates the direction orthogonal to the dominant CPL degeneracy, and corresponds to the redshift at which the dataset most directly constrains the EOS. For combined BAO+CMB+SNe samples, this typically lies near $z_p\simeq 0.4$ –0.6, close to the transition region where all three probes contribute comparable weight.

C. Bias equation under partial or inconsistent likelihoods

When multiple cosmological probes are combined, any mismatch in their effective likelihoods—arising from partial information, implicit priors, or differences in redshift sensitivity—can induce biased inferences of (ω_0, ω_a) even when the underlying cosmology is perfectly consistent with Λ CDM [39–42]. This behaviour can be quantified analytically. Suppose probe i has a small offset $\delta\theta_i$ between its intrinsic best-fit and the true fiducial parameters. In the Gaussian approximation, the shift of the joint posterior mean is given by

$$\Delta \boldsymbol{\theta} = F^{-1} \sum_{i} F_{i} \,\delta \boldsymbol{\theta}_{i},\tag{5}$$

where F_i is the Fisher matrix of probe i and $F = \sum_i F_i$ is the Fisher matrix of the combined system. Equation (5) shows that the total bias is a Fisher-weighted sum of individual shifts, with F^{-1} determining how the contributions from different probes project onto the final parameter space.

Each cosmological probe samples a different redshift regime and therefore constrains a different combination of (ω_0, ω_a) . Low-redshift SNe constrain the slope and curvature of $D_L(z)$ and thus anchor Ω_{m0} and w_0 , intermediate-redshift BAO constrain D_M/r_d and D_H/r_d , which depend more strongly on $\Omega_{m0} + \beta w_a$, and CMB distance priors

TABLE I. Qualitative parameter compensation required to maintain the same comoving distance $D_A(z_*)$ under a lower H_0 , extended to include the constraining effect of SNe luminosity distances.

Scenario	H_0	Ω_m	w_0	w_a
CMB-preferred (low H_0)		1	↑ (less negative)	<u> </u>
DESI BAO-preferred	↑	\downarrow	\downarrow	†
SNe constraint (low- z)	fix	\downarrow	tightens low-z slope	$tightens\ curvature$

probe a high-redshift combination of the form $\Omega_{m0} + \kappa w_a$ with $\kappa \simeq 0.6$ –0.8. Because these combinations differ, each probe has its own degeneracy ridge in the (ω_0, ω_a) plane, and these ridges are inherently misaligned due to distinct redshift sensitivities and distance-calibration anchors. Even small differences in their preferred cosmological parameters therefore move the ridge intersections to different locations in parameter space, producing apparent deviations from $(\omega_0, \omega_a) = (-1, 0)$.

Equation (5) makes clear that the induced bias $\Delta \theta$ follows the degeneracy direction of each probe. The product $F_i \, \delta \theta_i$ projects the misalignment onto the probe's principal eigenvectors, and F^{-1} then translates this into the bias of the combined posterior. Probes with long degeneracy ridges—such as BAO or CMB when analyzed without SNe—produce especially large shifts, even if $\delta \theta_i$ is small. This explains why partial likelihoods or compressed observables can generate spurious signatures of phantom crossing or DDE. SNe play a special role. They strongly constrain the low-redshift expansion history and therefore sharpen the projection orthogonal to the BAO+CMB degeneracy. As a result, the combined BAO+CMB+SNe analysis becomes highly sensitive to cross-probe inconsistencies, with even small offsets in (Ω_{m0}, H_0) across probes capable of inducing a substantial shifts in (ω_0, ω_a) .

In summary, parameter biases in multi-probe combinations arise not only from explicit tensions between datasets but also from the intrinsic geometry of their likelihoods. Partial or inconsistent likelihoods naturally lead to displaced posteriors through the mechanism encoded in Eq. (5), highlighting the importance of using fully consistent, covariance-aware likelihoods when interpreting potential evidence for DDE.

D. Geometric compensation in the CMB-BAO-SNe system

The CMB prefers a lower value of the Hubble constant relative to late-time probes such as BAO and SNe. To preserve the comoving angular-diameter distance to last scattering,

$$D_A(z_*) = \frac{c}{H_0(1+z_*)} \int_0^{z_*} \frac{dz'}{E(z')},\tag{6}$$

a lower H_0 must be compensated by a higher Ω_m or a less negative effective DE EOS. In the CPL form, approximate invariance of $D_A(z_*)$ implies

$$\omega_0 + \omega_a \simeq \text{const.},$$
 (7)

identifying the dominant degeneracy direction at high redshift.

BAO measurements break part of this degeneracy by constraining the ratio $D_V(z)/r_d$ at intermediate redshift. SNe add an additional lever arm through the luminosity distance, sensitive to the integral of 1/H(z) at low z. Including SNe therefore rotates and tightens the combined degeneracy contour, pulling the joint constraints toward the region that simultaneously satisfies the CMB acoustic scale, BAO distance ratios, and SNe low-redshift expansion history.

The net geometric compensation for a CMB-preferred lower H_0 is thus

$$H_0 \downarrow \Rightarrow \Omega_m \uparrow, \qquad \omega_0 \uparrow, \qquad \omega_a \downarrow,$$
 (8)

with SNe reducing the allowed variation in (ω_0, ω_a) by fixing the shape of H(z) at low redshift. Table I summarizes the qualitative trends.

III. MOCK LIKELIHOODS: DESI-LIKE BAO, PLANCK-LIKE CMB, AND PANTHEON-LIKE SNE

To perform a controlled null test of DDE inference, we construct fully self-consistent synthetic datasets for BAO, CMB distance priors, and SNe. All mock observables are generated from a single fiducial flat ΛCDM cosmology,

$$(\Omega_{m0}, H_0, w_0, w_a) = (0.30, 70 \,\text{km/s/Mpc}, -1, 0).$$
 (9)

Throughout the mock construction, the sound horizon is fixed to its fiducial value $r_d = (hr_d)/h = 147.1$ Mpc (corresponding to $hr_d = 103$ Mpc). This allows all probes to share a common acoustic scale, avoiding model-dependent variations. With this approach, the background expansion and comoving distances are defined uniformly across all probes. The quantities $D_M(z)$, $D_H(z)$, r_d , R, ℓ_A , and $\mu(z)$ are therefore internally consistent throughout the combined likelihood analysis.

A. DESI-like BAO: D_M/r_d and D_H/r_d

The mock BAO catalogue is constructed using the DESI DR2 redshift sampling and covariance structure [1, 2]. For each redshift bin z_i , we compute the fiducial cosmology predictions

$$D_M(z_i) = \int_0^{z_i} \frac{c \, dz'}{H(z')}, \qquad D_H(z_i) = \frac{c}{H(z_i)}, \tag{10}$$

and divide by the fiducial sound horizon r_d . These values are assembled into the vector

$$\mathbf{d}_{\text{fid}} = \left(D_M/r_d, \ D_H/r_d\right)_{\text{fid}}.\tag{11}$$

The observational covariance for each bin is taken directly from the DESI DR2 published tables, which report

$$\sigma^2(D_M/r_d), \quad \sigma^2(D_H/r_d), \quad \rho_{DM,DH}. \tag{12}$$

These are assembled into a $2N_z \times 2N_z$ block-diagonal covariance matrix with cross-terms in each block reflecting the DESI-measured correlation between transverse and radial modes. A correlated Gaussian realization is obtained by

$$\mathbf{d}_{\text{mock}} = \mathbf{d}_{\text{fid}} + L_{\text{BAO}}\mathbf{g},\tag{13}$$

where $L_{\rm BAO}$ is the Cholesky factor of the DESI DR2 covariance matrix and \mathbf{g} is a standard-normal vector [43–45]. The final BAO mock archive contains

$$\{z_i, (D_M/r_d)_{\text{mock}}, (D_H/r_d)_{\text{mock}}, C_{\text{BAO}}\},$$
 (14)

preserving the full DESI DR2 error model.

B. Planck-like CMB distance priors

For the CMB, we adopt a compressed Gaussian distance-prior likelihood that captures the leading geometric information from the acoustic scale while avoiding reliance on the full power-spectrum pipeline (see [31, 32] for detailed justification). This compressed prior retains nearly all the geometric constraining power relevant for late-time DE analyses and reproduces the parameter degeneracy directions of the full Planck likelihood to excellent accuracy. The CMB mock is defined in terms of the vector

$$\mathbf{v} = (R, \, \ell_A, \, \omega_b), \tag{15}$$

where the fiducial cosmology yields

$$R = \sqrt{\Omega_m H_0^2} D_M(z_*), \qquad \ell_A = \pi \frac{D_M(z_*)}{r_d}, \tag{16}$$

with $z_* \simeq 1089$ the redshift of the last scattering surface. The mock baryon density $\omega_b = \Omega_b h^2$ is fixed to its fiducial value. We use a Planck-like covariance matrix C_{CMB} with structure consistent with the Planck 2018 analysis [46], including the small but nonzero anticorrelation between R and ℓ_A . A correlated Gaussian realization is drawn via

$$\mathbf{v}_{\text{mock}} = \mathbf{v}_{\text{fid}} + L_{\text{CMB}}\mathbf{g},\tag{17}$$

with $L_{\rm CMB}$ the Cholesky factor of $C_{\rm CMB}$. The mock archive contains

$$\{\mathbf{v}_{\text{mock}}, \mathbf{v}_{\text{fid}}, C_{\text{CMB}}\}.$$
 (18)

C. Pantheon-like Supernovae with full covariance

The supernova mock dataset is based on the full Pantheon+SH0ES statistical plus systematic covariance matrix [6], which encodes correlations from calibration, Malmquist bias, dust modeling, and selection functions. We adopt the Pantheon+ redshift distribution $\{z_i\}$ and compute, for each supernova,

$$\mu_{\text{fid}}(z_i) = 5\log_{10}[D_L(z_i)] + M_B, \tag{19}$$

using the exact luminosity distance integral

$$D_L(z) = (1+z)\frac{c}{H_0} \int_0^z \frac{dz'}{E(z')}.$$
 (20)

To construct a realistic correlated mock, we use the full Pantheon+ covariance matrix $C_{\rm SN}$ and generate

$$\mu_{\text{mock}} = \mu_{\text{fid}} + L_{\text{SN}}\mathbf{g},\tag{21}$$

with $L_{\rm SN}$ the Cholesky factor of $C_{\rm SN}$. No explicit magnitude offset is injected because the true cosmology is known; the subsequent likelihood analysis marginalizes analytically over an additive offset parameter, following standard SN practice. The resulting archive contains

$$\{z_i, \ \mu_{\text{mock}}, \ C_{\text{SN}}\},\tag{22}$$

reproducing both the Pantheon+ redshift distribution and the full large-scale systematic calibration structure.

D. Combined likelihood and cross-probe consistency

Because all mock observables are generated from the same fiducial background cosmology and share a fully consistent definition of H(z), $D_M(z)$, $D_H(z)$, $D_L(z)$, and the fiducial sound horizon r_d , the BAO, CMB, and SNe mocks are mutually compatible by construction. Moreover, the likelihood analysis for each probe employs the actual DESI DR2, Planck 2018, and Pantheon+ covariance matrices, ensuring that both the mock generation and the subsequent MCMC inference incorporate realistic observational uncertainties and their full correlation structure. Consequently, the combined BAO+CMB+SNe likelihood contains no artificial cross-probe tension. Any apparent deviation from $(\omega_0, \omega_a) = (-1, 0)$ observed in our null-test analyses must originate solely from probe geometry, partial or compressed likelihoods, or misaligned degeneracy directions, rather than from inconsistencies in the mock dataset itself or from the treatment of covariances.

IV. MULTI-PROBE CONSTRAINTS FROM BAO, CMB, AND SNE MOCK DATA

In this section, we present the cosmological constraints obtained from the realistic mock datasets generated for BAO, CMB, and SNe Ia, based on the fiducial Λ CDM cosmology described in Sec. III. Our aim is to quantify how each individual probe and their various combinations constrain the parameter space $\{\Omega_{m0}, H_0, \omega_0, \omega_a\}$, and to determine whether the full multi-probe analysis successfully recovers the underlying fiducial cosmology.

We analyze seven cases: BAO only, CMB only, SNe only, BAO+CMB, BAO+SNe, CMB+SNe, and the full BAO+CMB+SNe combination. For each case, we perform an MCMC likelihood analysis using the appropriate covariance matrices for all observables, producing marginalized parameter constraints and two-dimensional posterior contours using GetDist [47]. As we demonstrate below, individual probes or pairwise combinations do not fully recover the fiducial parameters and can mimic signatures of DDE; however, the complete three-probe combination restores the input ΛCDM cosmology, consistent with the absence of any genuine inter-probe tension in the mock data.

A. BAO-only Constraints

We first analyze the BAO-only mock dataset generated from the fiducial Λ CDM cosmology. The parameters $\{\Omega_{m0}, H_0, \omega_0, \omega_a\}$ are sampled using the full DESI DR2 covariance matrix for the BAO distance indicators $\{D_M/r_d, D_H/r_d\}$ across all redshift bins. Because BAO observables constrain only the ratios D_M/r_d and D_H/r_d , rather than the absolute distance scale, the inference is intrinsically sensitive to the combination hr_d . Consequently, H_0 and H_0 cannot be independently determined from BAO information alone.

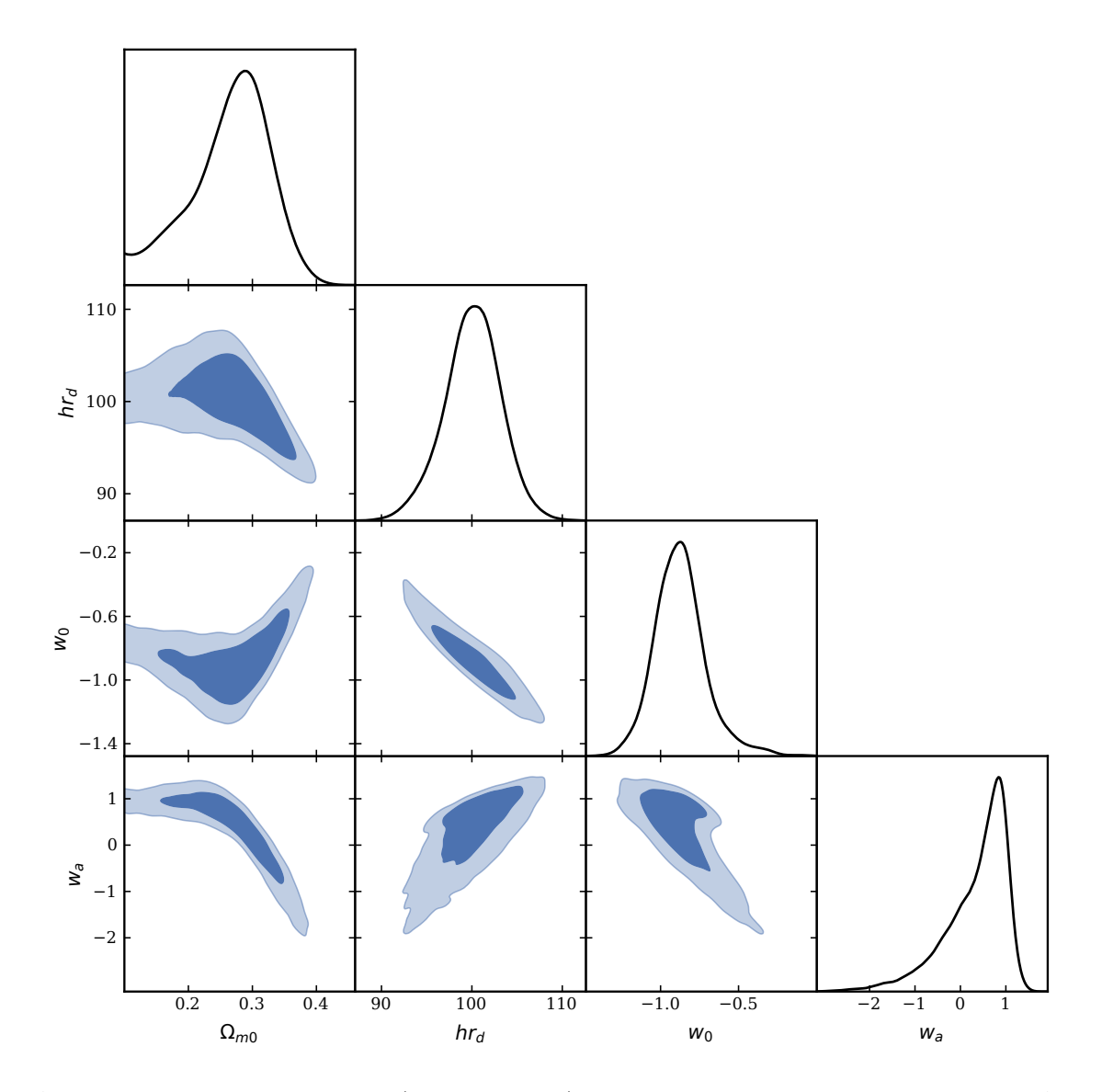


FIG. 1. BAO-only marginalized posteriors in $(\Omega_{m0}, hr_d, \omega_0, \omega_a)$, showing the characteristic degeneracies of BAO distances and their limited constraining power on DDE. The darker and lighter shaded regions indicate the 68% and 95% marginalized credible contours, respectively.

Figure 1 displays the resulting marginalized posteriors. As expected from BAO information alone, the constraints exhibit extended degeneracies in both the (H_0, Ω_{m0}) and (ω_0, ω_a) planes, reflecting the fact that D_M/r_d and D_H/r_d depend primarily on $E(z) = H(z)/H_0$ and the inverse sound-horizon scale. The marginalized 68% constraints are

$$\Omega_{m0} = 0.2650 \pm 0.0627, \quad H_0 = 100.04 \pm 3.19 \text{ km/s/Mpc},$$

$$\omega_0 = -0.8710 \pm 0.1720, \quad \omega_a = +0.3398 \pm 0.7084.$$
(23)

The corner plot in Fig. 1 highlights the characteristic degeneracy directions inherent to BAO measurements. The (Ω_{m0}, hr_d) plane shows the familiar Alcock–Paczynski (AP) anti-correlation that arises because BAO is a shape-only distance probe. It constrains the ratio of the transverse to radial clustering scales, but not the absolute expansion rate or the physical acoustic scale separately. The (ω_0, ω_a) plane exhibits a long, shallow degeneracy direction set by the limited late-time leverage of BAO distances on the redshift evolution of the DE EOS.

These degeneracies explain why BAO alone fails to recover the fiducial Λ CDM model. Even though the mock observables are generated from the fiducial cosmology, the combination of realistic DESI DR2 observational noise and the intrinsic BAO degeneracy structure allows the posterior to drift along the extended ridge direction in (ω_0, ω_a) . This behavior confirms that BAO provides precise geometric information but lacks the ability to isolate the time evolution of $\omega(z)$ without external information from CMB or SNe. Consequently, BAO alone cannot break the ω_0 - ω_a

degeneracy, and the recovered posterior naturally lies away from the fiducial $(\omega_0, \omega_a) = (-1, 0)$ point despite the underlying mock cosmology being exactly Λ CDM.

From the BAO-only chains we obtain the pivot EOS parameters

$$a_p = 0.8155,$$
 $z_p = a_p^{-1} - 1 = 0.2261,$ $\omega_p = -0.8083 \pm 0.1119.$ (24)

The fact that the BAO-only analysis correctly recovers $\omega_0 \simeq -1$ when ω_a is fixed, yet substantially deviates from the fiducial point when ω_a is allowed to vary, further emphasizes that BAO data do not contain sufficient information to constrain DDE. Once the additional degree of freedom introduced by ω_a is permitted, the likelihood elongates along the BAO degeneracy direction, causing the posterior to drift even for perfectly consistent Λ CDM mock data. This confirms that BAO distances constrain only specific combinations of $(H_0, \Omega_{m0}, \omega_0, \omega_a)$ and require complementary low-redshift (SNe) and high-redshift (CMB) probes to fully recover the underlying cosmology.

B. CMB-only Constraints

Next, we analyze the CMB-only mock dataset generated from the same fiducial Λ CDM cosmology. The four parameters $\{\Omega_{m0}, H_0, \omega_0, \omega_a\}$ are constrained using compressed CMB distance priors based on the acoustic scale ℓ_A , the shift parameter R, and the physical baryon density ω_b , following the standard Planck distance-prior formalism. These compressed quantities capture the leading geometric information encoded in the angular diameter distance to the last-scattering surface and the sound-horizon scale, but exclude the full CMB power-spectrum information. As a result, they preserve the well-known high-redshift geometric degeneracy between H_0 and Ω_{m0} and offer very limited sensitivity to late-time DE evolution.

Figure 2 shows the resulting marginalized posteriors. The CMB distance priors tightly constrain the angular acoustic scale and thus the combination $\Omega_{m0}h^2$, but they provide only an indirect projection of the low-redshift expansion history. As a consequence, the (H_0, Ω_{m0}) plane exhibits the familiar geometric degeneracy. Decreasing H_0 can be compensated by increasing Ω_{m0} while preserving the angular size of the sound horizon. Likewise, the (ω_0, wa) constraints form an extended ridge, reflecting the fact that the quantities (R, ℓ_A) depend almost entirely on the integral of 1/H(z) up to $z_* \simeq 1089$, where DE is dynamically negligible. Thus, CMB distance priors provide little direct information about the low-redshift behaviour of $\omega(z)$. The marginalized 68% constraints are

$$\Omega_{m0} = 0.3181 \pm 0.0809, \quad H_0 = 69.17 \pm 8.71 \text{ km/s/Mpc},$$

$$\omega_0 = -0.4633 \pm 0.5287, \quad \omega_a = -1.9887 \pm 1.7615.$$
(25)

From the CMB-only chains, we obtain the pivot equation-of-state parameters

$$a_p = 0.76245, z_p = 0.31157, \omega_p = -0.9355 \pm 0.3259.$$
 (26)

The deviation of ω_p from the fiducial value reflects the projection of the CMB geometric degeneracy onto the (ω_0, ω_a) subspace. Because the CMB distance priors probe only the high-redshift geometry, changes in ω_0 and ω_a that modify the low-redshift expansion history produce negligible changes in (R, ℓ_A) ; the likelihood is therefore nearly flat along the degeneracy direction where the angular acoustic scale remains fixed.

These considerations explain why the CMB-only posterior fails to recover the fiducial $(\omega_0, \omega_a) = (-1, 0)$ model, despite the mock data being generated from Λ CDM. The preferred region is shifted along the geometric degeneracy direction toward the phantom-like quadrant, not because of genuine dark-energy evolution, but because distance priors offer insufficient leverage on the low-redshift expansion history. Consequently, CMB-only constraints on (ω_0, ω_a) remain highly degenerate, and complementary information from BAO or SNe is required to break these degeneracies and recover the true underlying cosmology.

C. SNe-only Constraints

We next examine the constraints obtained from the SNe-only mock dataset. The free parameters in this case are $\{\Omega_{m0}, H_0, \omega_0, \omega_a, M\}$, where M is the absolute magnitude of SNe Ia. The likelihood is constructed from the full Pantheon+ + SH0ES covariance matrix, which includes both statistical and systematic uncertainties. Because the SN likelihood depends on the combination $\mu(z) = 5 \log_{10} D_L(z) + M$, supernovae constrain only relative luminosity distances and therefore do not determine the absolute scale of the Hubble diagram without an external distance anchor.

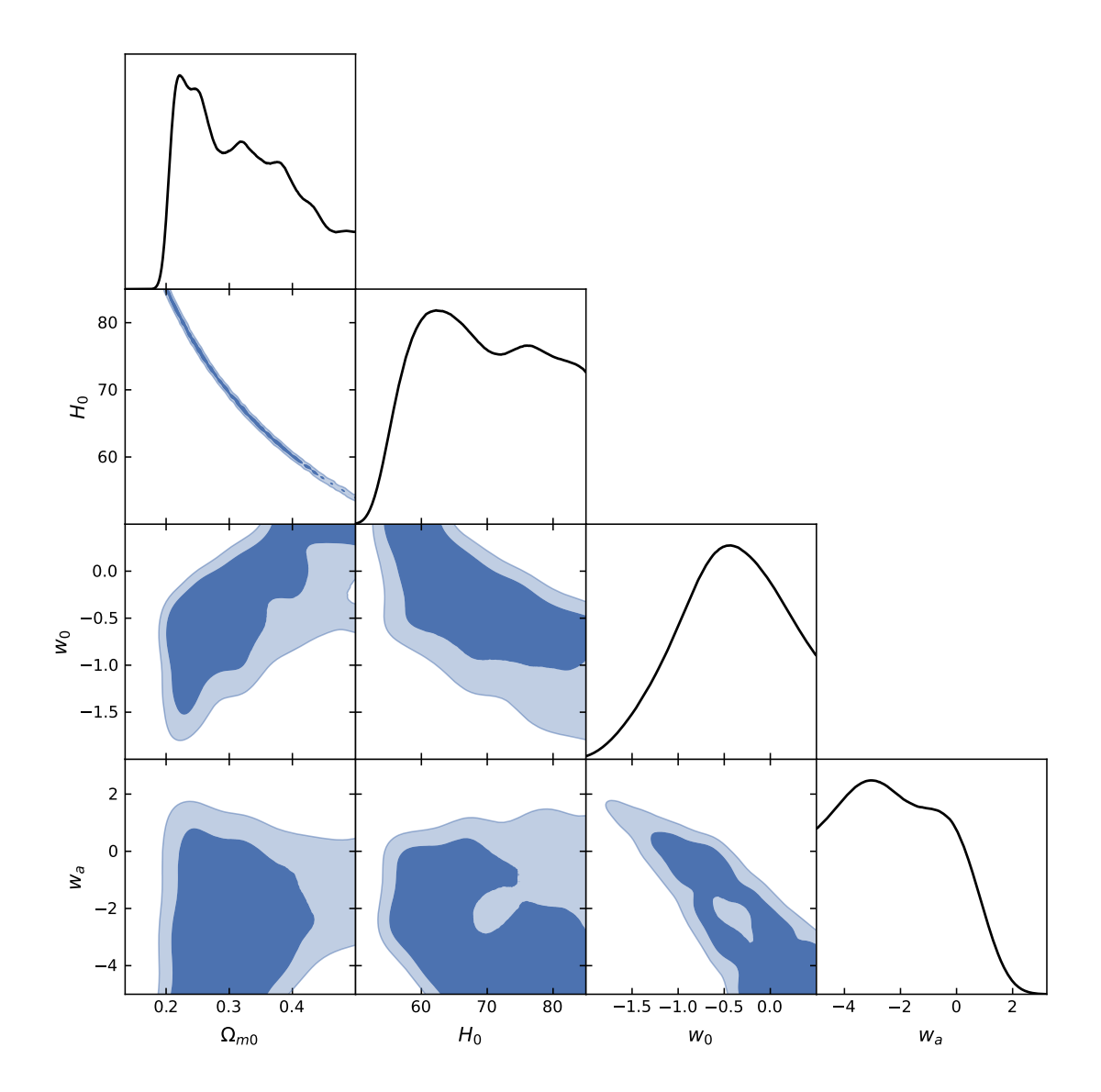


FIG. 2. CMB-only marginalized posteriors in $(\Omega_{m0}, H_0, \omega_0, \omega_a)$. Distance priors tightly constrain the high-redshift geometry but leave the late-time DE parameters weakly constrained, producing extended degeneracies in both (H_0, Ω_{m0}) and (ω_0, ω_a) .

Figure 3 displays the resulting posterior distributions. Because the luminosity distance scales as $D_L(z) \propto H_0^{-1}$, the SNe likelihood constrains only the combination $M - 5 \log_{10} H_0$, producing a pronounced degeneracy between H_0 and the absolute magnitude M. As a result, the absolute expansion scale is left essentially unconstrained.

The DE parameters (ω_0, ω_a) are likewise only weakly constrained. Luminosity distances depend on the integral of 1/H(z), and SNe probe only the low-redshift regime $(z \leq 1)$, where changes in DE parameters can be compensated along a broad degeneracy direction. Consequently, the (ω_0, ω_a) posterior forms an elongated ridge reflecting the limited ability of SNe to isolate the detailed evolution of $\omega(z)$ without complementary information from BAO or CMB. The marginalized 68% constraints are

$$\Omega_{m0} = 0.3447 \pm 0.0977,$$
 $H_0 = 73.11 \pm 11.37 \text{ km/s/Mpc},$ $w_0 = -1.3198 \pm 0.2170,$ $w_a = +0.4688 \pm 1.3098,$ $M = 0.0574 \pm 0.3438.$ (27)

From the SNe-only chains we obtain the pivot equation-of-state parameters

$$a_p = 1.0384, z_p = -0.0370, w_p = -1.3378 \pm 0.2110.$$
 (28)

The negative pivot redshift reflects the extremely weak leverage of SNe-only data on the redshift evolution of the DE

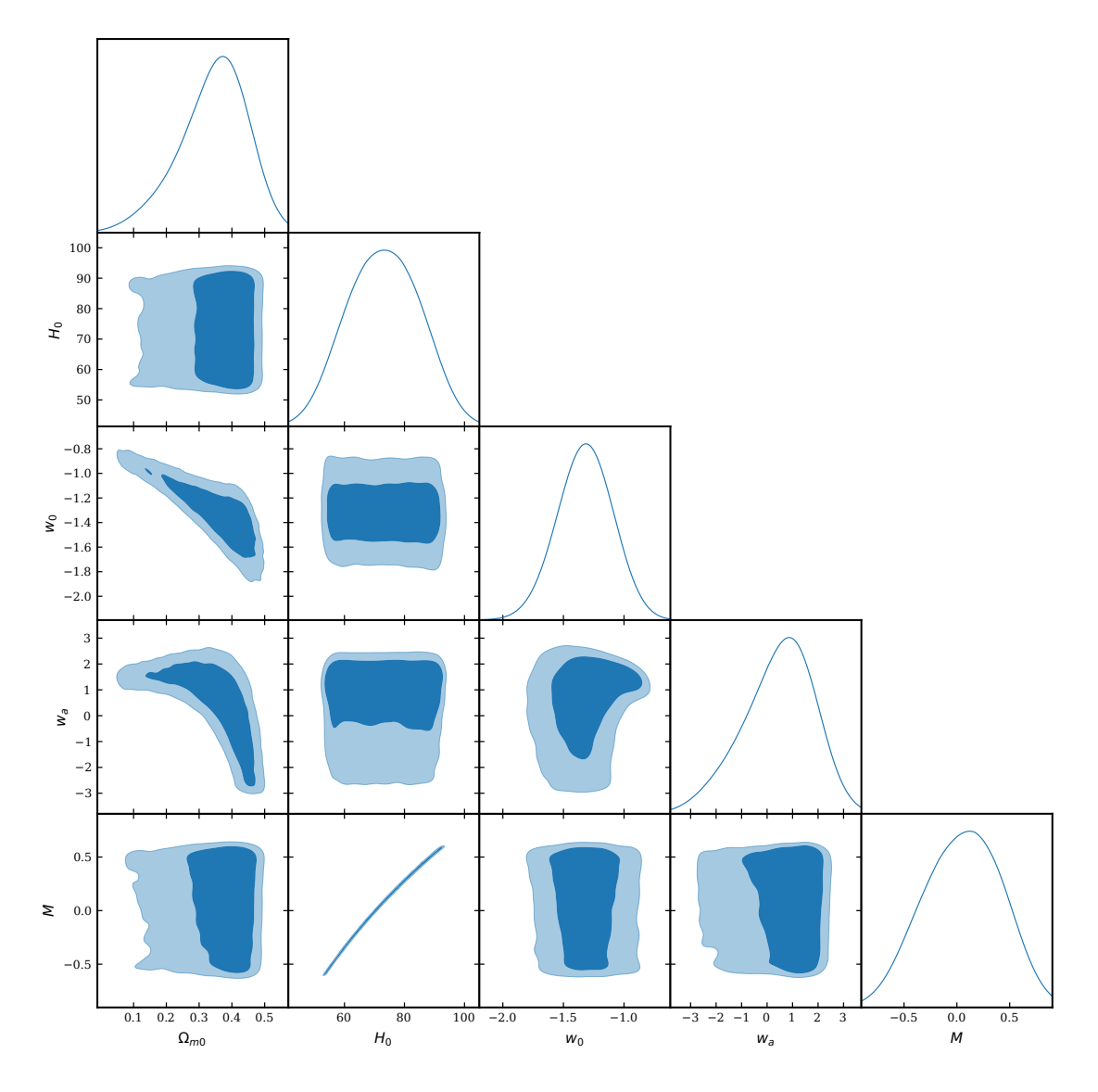


FIG. 3. Marginalized posteriors for the SNe-only mock dataset. Relative luminosity distances fix the Hubble diagram shape but not its normalization, yielding a pronounced (H_0, M) degeneracy and an elongated ridge in (ω_0, ω_a) .

EOS, causing the pivot to lie outside the observable range. This behaviour is expected for SNe in the absence of an external distance calibration.

Overall, these results show that SNe alone cannot recover the fiducial model. The SNe-only posterior is shifted along the characteristic SN degeneracy direction, highlighting the shape-only nature of SNe distances and reinforcing the need for complementary BAO or CMB measurements to break degeneracies and robustly reconstruct the late-time expansion history.

D. Joint BAO+CMB Constraints

In this subsection, we examine the constraints obtained from combining the DESIDR2 BAO measurements and the Planck 2018 compressed CMB distance priors. The joint likelihood is constructed as

$$\chi_{\text{tot}}^2 = \chi_{\text{BAO}}^2 + \chi_{\text{CMB}}^2, \tag{29}$$

where $\chi^2_{\rm BAO}$ uses the full DESIDR2 covariance of $(D_M/r_d, D_H/r_d)$ and $\chi^2_{\rm CMB}$ incorporates the compressed distance priors (R, ℓ_A, ω_b) and their covariance. Sampling is performed over the five-dimensional parameter space $(\Omega_{m0}, H_0, \omega_0, \omega_a, r_d)$, with the sound horizon r_d recalculated at each MCMC step.

Parameter	Best-fit	68% credible interval
Ω_{m0}	0.412	$0.411^{+0.011}_{-0.011}$
$H_0 [{\rm km s^{-1} Mpc^{-1}}]$	58.26	$58.33^{+0.066}_{-0.44}$
ω_0	-3.53×10^{-4}	$-3.84^{+2.89}_{-6.31} \times 10^{-3}$
ω_a	-1.854	$-1.849^{+0.091}_{-0.092}$
$r_d (\mathrm{Mpc})$	179.999	$179.954^{+0.349}_{-1.181}$

TABLE II. Marginalized posterior constraints from the joint BAO+CMB likelihood, derived from the MCMC chain. Uncertainties denote the 16th and 84th percentiles.

The marginalized constraints derived from the MCMC chain are summarized in Table II. For each parameter, we report the maximum-likelihood value (MLV) together with the 16th–84th percentile credible interval obtained from the one-dimensional marginalized posterior. This percentile range corresponds to the central 68% credible interval of the marginalized distribution and is generally asymmetric around the MLV. These intervals are obtained by marginalizing the full five-dimensional posterior over $(\Omega_{m0}, H_0, \omega_0, \omega_a, r_d)$, and therefore reflect the central 68% credible region implied by the compelete joint likelihood. Numerically, the joint BAO+CMB likelihood prefers a relatively high matter density, $\Omega_{m0} \simeq 0.41$, and a low Hubble constant, $H_0 \simeq 58 \text{ km s}^{-1} \text{ Mpc}^{-1}$, consistent with the well-known CMB geometric degeneracy. The CPL parameters exhibit a strongly constrained combination: ω_0 is tightly pulled toward zero while ω_a is driven to $\omega_a \simeq -1.85$, indicating a steeply evolving phantom-like trajectory in the (ω_0, ω_a) plane. The sound horizon is correspondingly shifted to a larger value, $r_d \simeq 180 \text{ Mpc}$, fully consistent with the preference for lower H_0 and higher Ω_{m0} . Together, these results illustrate the strong constraining power of the BAO+CMB combination and the way in which their complementary geometrical information shapes the allowed CPL parameter space.

Although the joint BAO+CMB analysis yields a value of ω_0 very close to zero, this should not be interpreted as evidence for a non-accelerating universe. Instead, the appearance of $\omega_0 \simeq 0$ is a direct consequence of the statistical and geometrical degeneracy structure inherent to the combined BAO+CMB likelihood. Both probes constrain the CPL DE EOS primarily through a specific high-redshift weighted combination,

$$\omega_{\text{eff}} \approx \omega_0 + \kappa \, \omega_a,$$
 (30)

with $\kappa \sim 0.6$ –0.8 for the redshift range relevant to the CMB acoustic scale. Along this degeneracy direction, a wide family of (ω_0, ω_a) pairs produce nearly identical distance measures, causing the posterior to drift toward solutions such as $(\omega_0 \approx 0, \omega_a \approx -1.8)$ even when the mock data were generated from the fiducial $(\omega_0, \omega_a) = (-1, 0)$. Thus, the value $\omega_0 \simeq 0$ reflects the geometry of the likelihood rather than any physical preference for a non-accelerating cosmology, and disappears once lower-redshift distance information (e.g., SNe Ia) is added to break the ω_0 – ω_a degeneracy.

Figure 4 shows the GetDist triangle plot of the joint BAO+CMB posterior in the parameter space. Compared with the BAO-only constraints, the inclusion of the Planck 2018 distance priors dramatically reduces the allowed volume of the CPL parameter space, producing compact, nearly Gaussian contours. In particular, the characteristic positive correlation between ω_0 and ω_a is clearly visible, reflecting the CMB acoustic-scale degeneracy direction. The plot also illustrates how the joint likelihood pushes the posterior toward high Ω_{m0} , low H_0 , and correspondingly larger r_d , consistent with the geometric preference identified above. This visualization highlights the strong constraining power of the combined BAO+CMB dataset and its role in shaping the joint (ω_0, ω_a) posterior ridge.

From the MCMC chain we obtain

$$\omega_p^{(16)} = -0.0239, \quad \omega_p^{(50)} = -0.0176, \quad \omega_p^{(84)} = -0.0148,$$
 (31)

indicating that the joint BAO+CMB likelihood tightly constrains the high-signal-to-noise pivot combination and significantly reduces the allowed CPL parameter volume compared to the single-probe analyses.

The combined BAO+CMB constraints demonstrate the power of coupling the high-redshift CMB acoustic scale with the low-redshift BAO distance ratios. The CMB priors effectively fix the absolute distance scale and the early-time expansion, while BAO provides precise intermediate-redshift geometry. Together these datasets break the broad degeneracies present in the individual BAO-only and CMB-only analyses, producing tight constraints and yielding a robust anchor for the full multi-probe cosmological analysis.

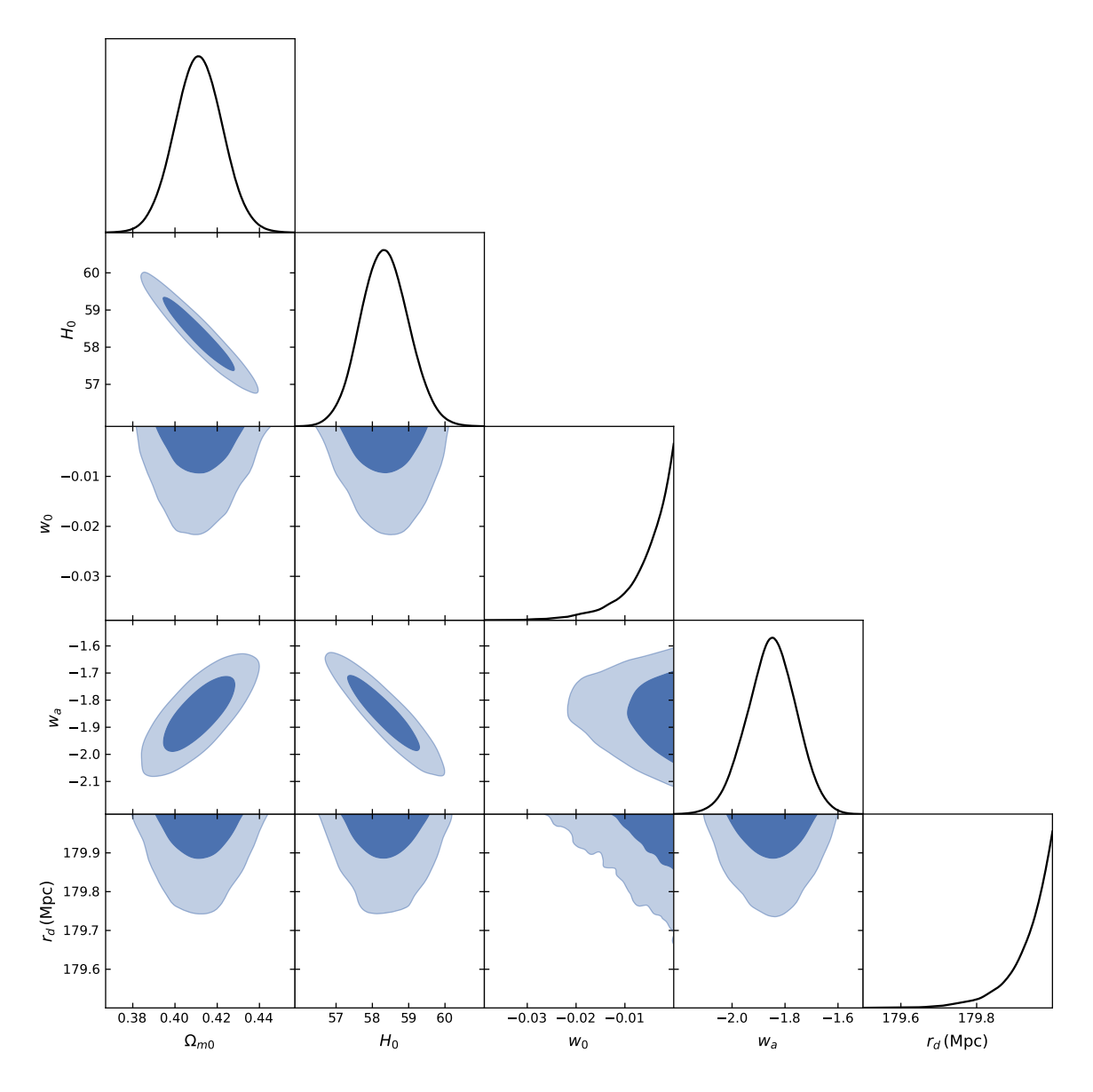


FIG. 4. Joint BAO+CMB posterior distributions for $(\Omega_{m0}, H_0, \omega_0, \omega_a, r_d)$ from the GetDist analysis. The Planck 2018 distance priors tighten the parameter constraints and produce the characteristic positive ω_0 – ω_a correlation associated with the CMB acoustic-scale degeneracy.

E. Joint BAO+SNe Constraints

We now combine the DESIDR2 BAO distance measurements with the Pantheon+ supernova luminosity-distance data to constrain the parameter space $(\Omega_{m0}, H_0, \omega_0, \omega_a)$. The joint likelihood is given by

$$\chi_{\text{tot}}^2 = \chi_{\text{BAO}}^2 + \chi_{\text{SNe}}^2, \tag{32}$$

where $\chi^2_{\rm BAO}$ is constructed from the DESIDR2 covariance of $(D_M/r_d, D_H/r_d)$ and $\chi^2_{\rm SNe}$ uses the full Pantheon+statistical and systematic covariance matrix. The sampling is performed in the four-dimensional parameter space, with the supernova absolute magnitude consistently marginalized using the Pantheon+ formalism.

The marginalized constraints from the MCMC chain are summarized in Table III. For each parameter, we quote the MLV together with the 16th–84th percentile credible interval from the one-dimensional marginalized posterior. Numerically, the BAO+SNe combination favors a relatively low matter density, $\Omega_{m0} \simeq 0.24$, and a Hubble constant near the SH0ES scale, $H_0 \simeq 70 \text{ km s}^{-1} \text{ Mpc}^{-1}$. The CPL parameters are driven close to the fiducial cosmology, with $\omega_0 \simeq -1.03$ and a mildly positive $\omega_a \simeq +1.0$, reflecting the increased constraining power obtained by linking

Parameter	Best-fit	68% credible interval
Ω_{m0}	0.230	$0.238^{+0.037}_{-0.059}$
$H_0 [{\rm km s^{-1} Mpc^{-1}}]$	70.157	$70.108^{+0.220}_{-0.217}$
ω_0	-1.033	$-1.028^{+0.080}_{-0.057}$
ω_a	1.007	$0.968^{+0.142}_{-0.291}$

TABLE III. Marginalized posterior constraints from the joint BAO+SNe likelihood. Values denote ML estimates and 16th–84th percentile credible intervals from the one-dimensional marginalized posterior.

low-redshift luminosity distances with intermediate-redshift BAO geometry.

Using the MCMC samples, we obtain the pivot combination

$$\omega_p^{(16)} = -1.031, \quad \omega_p^{(50)} = -1.020, \quad \omega_p^{(84)} = -1.009,$$
 (33)

demonstrating that BAO+SNe tightly constrain the low-to-intermediate redshift combination ω_p along the maximum-signal direction.

Figure 5 displays the full multidimensional posterior of the joint BAO+SNe likelihood. Compared with the individual BAO-only and SNe-only analyses, the combination produces significantly more compact contours. BAO geometry constrains the intermediate-redshift expansion, while SNe anchor the low-z luminosity-distance relation, leading to a well-localized region in the (ω_0, ω_a) plane. The positive correlation between ω_0 and ω_a reflects the characteristic BAO degeneracy direction, while the SNe data pull ω_0 tightly toward -1, together yielding a preferred region near $\omega_0 \approx -1$ and mildly positive ω_a .

The preference of the joint BAO+SNe constraints for $(\omega_0 \simeq -1, \omega_a > 0)$ arises from the complementary redshift sensitivities and degeneracy structures of the two probes. Supernova luminosity distances precisely determine the shape of the low-redshift expansion history and therefore anchor ω_0 tightly near -1, while being only weakly sensitive to the time evolution encoded in ω_a . Conversely, BAO distances probe the intermediate-redshift regime $(0.3 \lesssim z \lesssim 1.5)$, where DE evolution contributes mainly through the combination $\omega_0 + \beta \omega_a$ with $\beta \sim 0.5$, making BAO relatively more sensitive to ω_a than to ω_0 . Because the dominant SNe and BAO degeneracy directions are nearly orthogonal in the (ω_0, ω_a) plane, their intersection selects a narrow region close to $\omega_0 = -1$ and slightly positive ω_a . Mathematically, this reflects the different functional dependences of the distance integrals on ω_0 and ω_a , which, when combined, efficiently break the broad degeneracies present in the individual datasets and yield a well-localized CPL solution consistent with the BAO+SNe posterior.

The joint BAO+SNe likelihood thus provides a long redshift lever arm linking the low and intermediate redshifts, significantly tightening the CPL constraints and driving the posterior toward a region close to the fiducial expansion history. These results illustrate the essential role of SNe in anchoring the absolute distance scale and breaking the ω_0 – ω_a degeneracy when combined with BAO measurements.

F. Joint CMB+SNe Constraints

We now combine the Planck 2018 CMB distance priors with the Pantheon+ supernova luminosity-distance measurements to constrain the CPL parameter space $(\Omega_{m0}, H_0, \omega_0, \omega_a)$. The joint likelihood is defined as

$$\chi_{\text{tot}}^2 = \chi_{\text{CMB}}^2 + \chi_{\text{SNe}}^2,\tag{34}$$

where χ^2_{CMB} uses the compressed parameters (R, ℓ_A, ω_b) and their covariance, and χ^2_{SNe} employs the full Pantheon+ statistical and systematic covariance matrix. Sampling is performed over the four-dimensional parameter space, with the absolute SN magnitude consistently marginalized following the Pantheon+ procedure.

The marginalized posterior constraints are summarized in Table IV. For each parameter, we report the ML estimate together with the 16th–84th percentile credible interval. Numerically, the joint CMB+SNe combination yields a matter density close to the fiducial value, $\Omega_{m0} \simeq 0.295$, and a Hubble constant aligned with the SNe determination, $H_0 \simeq 70$ km/s/Mpc. The resulting CPL parameters modestly prefer $\omega_0 \simeq -1.09$ and $\omega_a \simeq +0.4$, reflecting the complementary information supplied by the early- and late-time distance constraints.

Using the MCMC samples, the pivot EOS parameter is tightly constrained

$$\omega_p^{(16)} = -0.9896, \quad \omega_p^{(50)} = -0.9744, \quad \omega_p^{(84)} = -0.9596,$$
 (35)

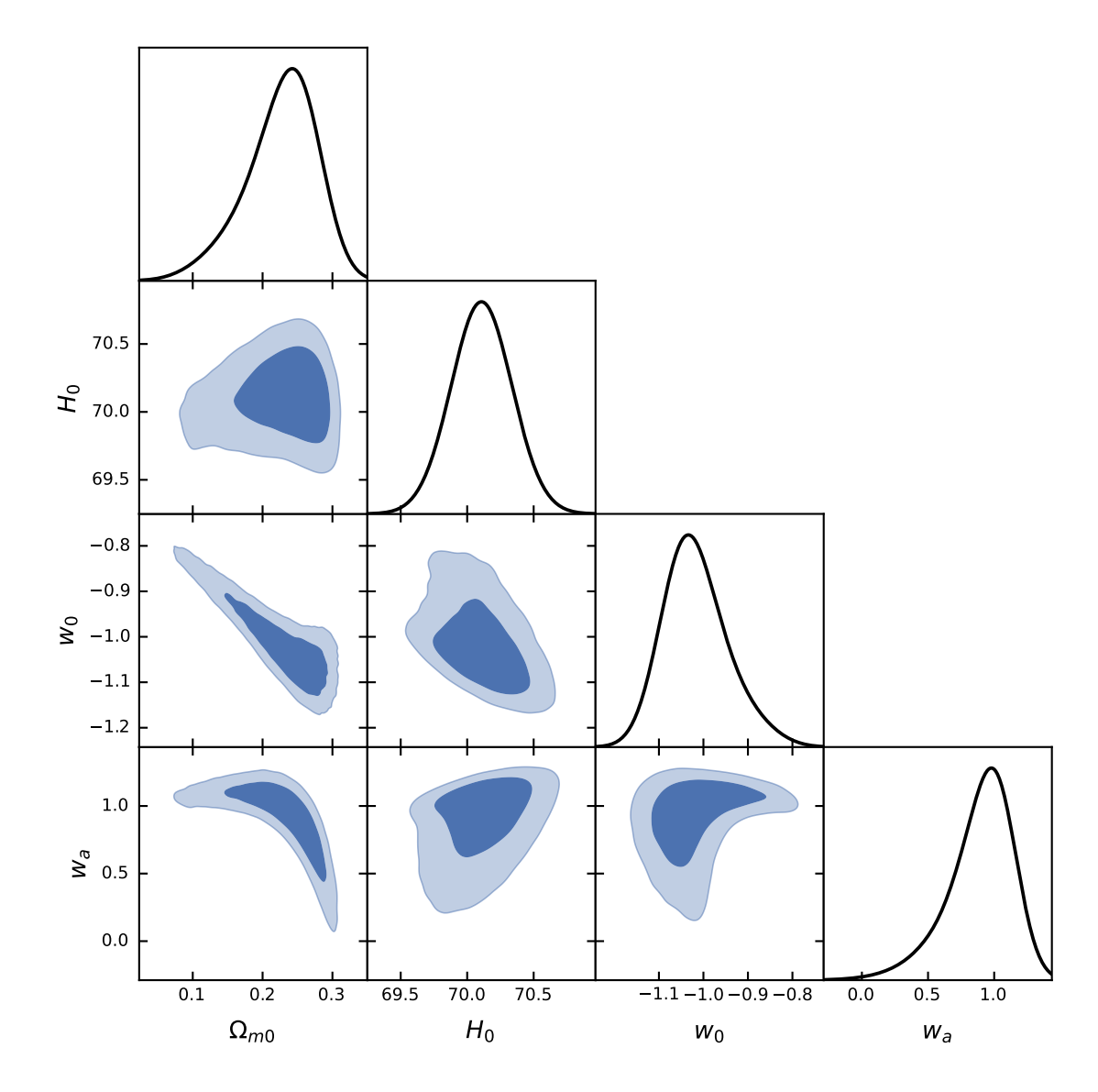


FIG. 5. GetDist triangle plot for the joint BAO+SNe posterior using BAO + SNe chains. The combination of intermediate-redshift BAO geometry with low-redshift supernova distances efficiently breaks the principal SNe degeneracy and yields significantly tighter contours than either dataset alone.

Parameter	Best-fit	68% credible interval
Ω_{m0}	0.294	$0.295^{+0.0035}_{-0.0035}$
$H_0 [\mathrm{km/s/Mpc}]$	70.148	$70.137^{+0.284}_{-0.280}$
ω_0	-1.097	$-1.094^{+0.061}_{-0.060}$
ω_a	0.395	$0.381^{+0.179}_{-0.189}$

TABLE IV. Marginalized posterior constraints from the joint CMB+SNe likelihood. Uncertainties denote the 16th–84th percentile credible intervals from the marginalized posterior.

indicating that the CMB+SNe likelihood provides strong constraints on the maximum-sensitivity combination ω_p , dominated by the interplay between the high-redshift CMB anchor and the low-redshift SNe distances.

Figure 6 shows the GetDist triangle plot for the joint CMB+SNe posterior. The CMB distance priors anchor the early-time geometry through the acoustic scale, constraining a specific high-redshift combination of the CPL parameters. SN distances, in contrast, tightly determine the shape of the low-redshift expansion history. Their

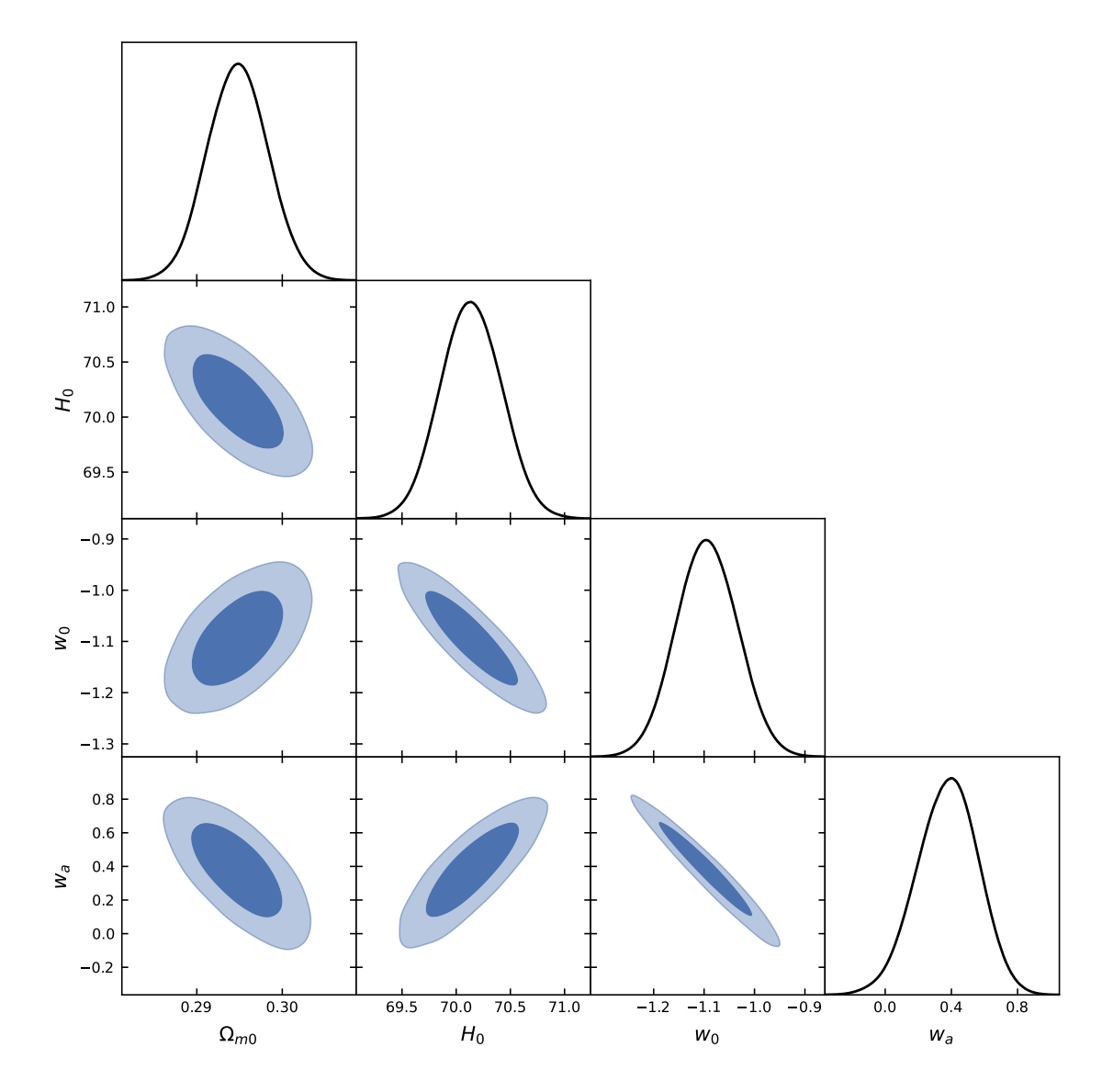


FIG. 6. Joint CMB+SNe posterior distributions for $(\Omega_{m0}, H_0, \omega_0, \omega_a)$. The CMB acoustic-scale prior anchors the high-redshift geometry, while the low-redshift SNe distances break the remaining degeneracies, producing compact and nearly orthogonal contours in the (ω_0, ω_a) plane.

combination produces nearly orthogonal degeneracy directions in the (ω_0, ω_a) plane, resulting in compact, well-localized contours that significantly tighten the allowed parameter space relative to either probe alone.

The preference of the joint CMB+SNe analysis for $(\omega_0 \lesssim -1, \omega_a > 0)$ follows directly from the complementary redshift sensitivities and nearly orthogonal degeneracy directions of the two probes. CMB distance priors constrain a high-redshift combination of the CPL parameters, $\omega_0 + \kappa \omega_a$ with $\kappa \sim 0.6$ –0.8, which naturally leads to a shallow degeneracy extending into the phantom-like region $\omega_0 < -1$. Supernovae, in contrast, tightly constrain the low-redshift expansion history and therefore pull ω_0 toward values near -1, while providing only weak constraints on ω_a . The intersection of these two degeneracy directions selects a narrow region with ω_0 slightly below -1 and mildly positive ω_a , fully consistent with Λ CDM within the 95% confidence region.

Overall, the joint CMB+SNe likelihood provides a long lever arm linking the low-z and high-z Universe, sharply tightening the CPL constraints and yielding a well-localized posterior that reflects the combined power of early- and late-time distance measurements.

Parameter	Best-fit	68% credible interval
Ω_{m0}	0.296	$0.296^{+0.0033}_{-0.0032}$
$H_0 [{\rm km s^{-1} Mpc^{-1}}]$	69.948	$69.940^{+0.226}_{-0.224}$
ω_0	-1.047	$-1.044^{+0.042}_{-0.039}$
ω_a	0.252	$0.238^{+0.126}_{-0.135}$

TABLE V. Marginalized posterior constraints from the joint BAO+CMB+SNe likelihood. Uncertainties denote the 16th–84th percentile credible intervals from the marginalized posterior.

G. Joint BAO+CMB+SNe Constraints

We now combine the DESI DR2 BAO distance measurements, the Planck 2018 compressed CMB distance priors, and the Pantheon+ supernova luminosity-distance data to obtain the most stringent constraints on the CPL parameter space $(\Omega_{m0}, H_0, \omega_0, \omega_a)$. The joint likelihood is defined as

$$\chi_{\text{tot}}^2 = \chi_{\text{BAO}}^2 + \chi_{\text{CMB}}^2 + \chi_{\text{SNe}}^2, \tag{36}$$

where each term constructed from the full covariance matrix for the corresponding dataset. Sampling is performed jointly over $(\Omega_{m0}, H_0, \omega_0, \omega_a)$, using the BAO+CMB+SNe chain.

The marginalized posterior constraints are presented in Table V. For each parameter, we quote the MLV together with the 1-sigma confidence level. Numerically, the fully joint dataset yields a matter density near the fiducial value, $\Omega_{m0} \simeq 0.296$, and a Hubble constant consistent with the SNe anchoring, $H_0 \simeq 69.94~{\rm km\,s^{-1}\,Mpc^{-1}}$. The CPL parameters are tightly constrained to $\omega_0 \simeq -1.04$ and $\omega_a \simeq +0.24$, values that lie extremely close to the fiducial $(\Omega_{m0}, H_0, w_0, w_a) \simeq (0.30, 70~{\rm km/s/Mpc}, -1, 0)$ model used to generate the mock data. This demonstrates that the full three-probe combination not only provides the smallest statistical uncertainties, but also most faithfully reconstructs the underlying fiducial cosmology by eliminating the degeneracies present in the individual BAO, CMB, and SNe analyses.

The pivot EOS parameter is tightly constrained by the combined dataset

$$\omega_p^{(16)} = -1.020, \quad \omega_p^{(50)} = -1.013, \quad \omega_p^{(84)} = -1.006,$$
 (37)

demonstrating the exceptional precision of the joint BAO+CMB+SNe analysis near the pivot redshift.

Figure 7 displays the GetDist triangle plot of the joint posterior. The figure illustrates how the three probes contribute complementary geometric information across widely separated redshift ranges. The CMB anchors the early-time acoustic scale through the combination $\omega_0 + \kappa \omega_a$ ($\kappa \sim 0.6$ –0.8), BAO distances determine the intermediate-redshift expansion via a distinct combination of (ω_0, ω_a), and SNe precisely constrain the shape of the low-redshift luminosity–distance relation. Because these three degeneracy directions intersect in a small region of the (ω_0, ω_a) plane, the contours collapse into compact, nearly Gaussian shapes centered near the fiducial (ω_0, ω_a) = (-1,0) model.

The behavior of the joint BAO+CMB+SNe posterior follows directly from the complementary redshift sensitivities and nearly orthogonal degeneracy directions of the three probes. CMB distance priors constrain a high-redshift weighted combination $\omega_0 + \kappa \omega_a$ and strongly favor the fiducial early-universe normalization, SNe anchor the low-redshift expansion history and pull ω_0 toward -1, and BAO distances determine the intermediate-redshift geometry with additional sensitivity to ω_a and Ω_{m0} . When combined, these three degeneracy structures intersect in a very small region of the full parameter space, causing the joint posterior to collapse toward the fiducial cosmology. Thus, the BAO+CMB+SNe combination provides the most accurate geometric reconstruction of the late-time expansion history and yields the tightest and most faithful recovery of the fiducial ACDM model among all probe combinations considered in this work. An important implication of this null test is that the current observational precision of the three probes is already sufficient to recover the underlying cosmological model with remarkable accuracy, provided that the datasets are mutually consistent. Because the three probes constrain nearly orthogonal combinations of parameter space across low, intermediate, and high redshifts, any genuine concordance among their covariance-weighted distance measurements forces the joint likelihood to collapse onto an extremely small region of the four-dimensional parameter space. Thus, in the absence of real physical tension among the probes, the BAO+CMB+SNe combination possesses the statistical power to faithfully reconstruct the true background expansion history of the Universe, yielding a near-exact recovery of the fiducial Λ CDM parameters used in the mock analysis.

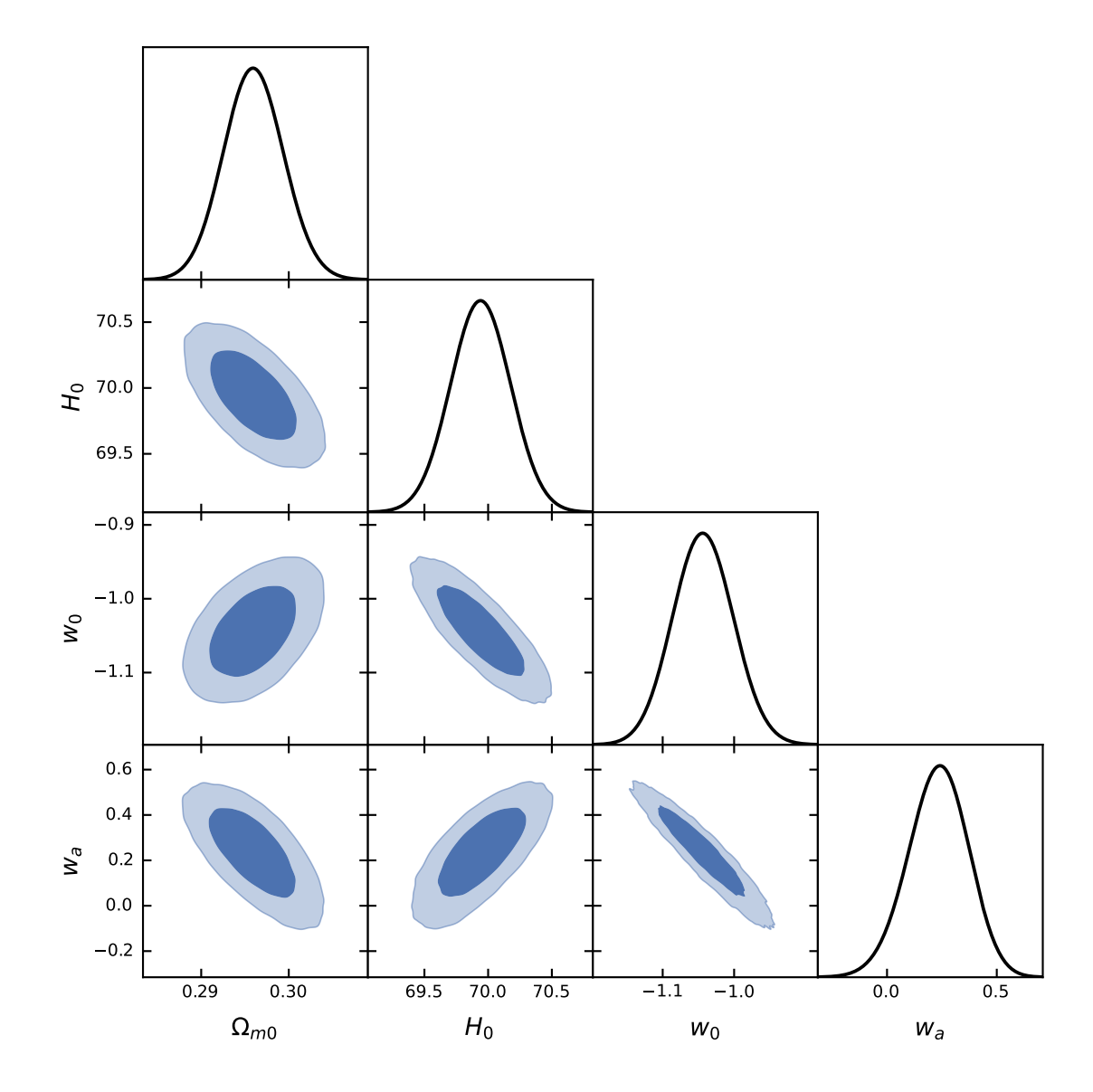


FIG. 7. Joint BAO+CMB+SNe posterior distributions for $(\Omega_{m0}, H_0, w_0, w_a)$. The three-probe combination eliminates the degeneracies present in individual and two-probe analyses, yielding a compact posterior that accurately reconstructs the fiducial Λ CDM model.

H. Comparative Constraints from All Probe Combinations

To compare how each observational probe constrains the CPL parameter space, we produce DESI-style GetDist overlay plots for all seven possible combinations of the three datasets:

These overlays provide a unified visualization of the degeneracy directions and relative constraining power associated with each probe and probe combination.

BAO primarily constrains the dimensionless distance ratios D_M/r_d and D_H/r_d and therefore exhibits strong correlations between (Ω_{m0}, H_0) but a weak response in the dark–energy sector (ω_0, ω_a) . CMB distance priors tightly restrict the physical matter density and acoustic scale, generating narrow constraints along the CMB geometric degeneracy direction in the (ω_0, ω_a) plane. SNe constrain the relative luminosity distance at low redshift and thus provide tight bounds on the late–time expansion rate, but are almost insensitive to r_d , producing extended degeneracies in (H_0, Ω_{m0}) .

By overlaying all seven probe combinations, we find that the three primary datasets exhibit highly complementary

degeneracy structures. In the (ω_0, ω_a) plane, BAO, CMB, and SNe produce almost orthogonal degeneracy directions, and the intersection of these directions significantly reduces the allowed parameter space for DDE. Two-probe combinations such as BAO+CMB, BAO+SNe, or CMB+SNe already tighten constraints relative to any single data set, although residual degeneracies remain visible in all cases. The full three-probe combination BAO+CMB+SNe yields the smallest contours in every two-parameter projection considered here, representing the highest level of constraining power attainable within the CPL framework.

While these idealized overlays assume mutually consistent probes, real data may exhibit internal tensions that distort the combined likelihood. In particular, recent studies have identified a mismatch between the Ω_{m0} preferred by Pantheon+ supernova data and that inferred from DESI DR2 BAO measurements. As shown in Ref. [10], imposing an SNe-preferred prior (e.g., $\Omega_{m0}=0.33$) on BAO data generated under a true Λ CDM cosmology ($\Omega_{m0}=0.30, \omega_0=-1, \omega_a=0$) induces substantial artificial shifts such as $\omega_0\simeq -0.82$ and $\omega_a\simeq -0.82$. These shifts resemble those reported in recent DESI DR2 BAO + Pantheon+ analyses, suggesting that apparent deviations from Λ CDM may arise from prior-induced statistical biases rather than new physics. Thus, although the overlays presented here illustrate the idealized case of internally consistent probes, real-data applications must carefully account for possible Ω_{m0} tension before interpreting deviations in (ω_0, ω_a) as physical.

Figures 8-11 present the four principal two-parameter projections of all seven probe combinations. Each of these triangle projections provides complementary information regarding how the individual and joint datasets constrain different directions in parameter space. As these four projections clearly show, when the three probes are mutually consistent and free of internal tensions, the combined BAO+CMB+SNe likelihood rapidly collapses toward a small region surrounding the fiducial cosmology, yielding convergent constraints that are fully consistent with the jointanalysis result shown in Fig. 7. Below we summarize the most salient features of each projection. Fig. 8 (i.e., (ω_0, ω_a) -plane) is the primary diagnostic plane for identifying signatures of DDE. BAO, CMB, and SNe each generate distinct degeneracy directions: BAO is nearly insensitive to w_a and mildly sensitive to ω_0 , while SNe tightly constrain a low-redshift combination of (ω_0, ω_a) , and CMB imposes a long, narrow geometric degeneracy. The near-orthogonality of these three directions explains why the BAO+CMB+SNe contour closes so efficiently in the joint analysis. However, as emphasized earlier, these idealized contours assume Ω_{m0} consistency across probes; real-data tensions can produce spurious rotations or shifts mimicking an evolving DE EOS. Fig. 9 (i.e., (Ω_{m0}, H_0))-plane) shows that distance–ratio BAO measurements dominate this plane because both D_M/r_d and D_H/r_d depend sharply on (Ω_{m0}, H_0) . CMB constrains a direction correlated with the physical matter density $\Omega_m h^2$, resulting in an elongated contour that intersects the BAO degeneracy at a nontrivial angle. SNe alone show a broad degeneracy aligned with the low-zluminosity-distance relation and constrain H_0 only weakly in the absence of an absolute calibration. The overlap of BAO and CMB is therefore essential for pinning down the (Ω_{m0}, H_0) pair with high precision. Fig. 10 (i.e., (w_0, Ω_{m0}) plane) highlights the key three-way interplay between matter density, dark-energy behavior, and geometric distance data. BAO couples Ω_{m0} and ω_0 through the AP relation, while SNe constrain an orthogonal direction dominated by the deceleration parameter combination $q_0 = \frac{1}{2}\Omega_{m0} + \frac{3}{2}(1+\omega_0)(1-\Omega_{m0})$. CMB adds a further independent degeneracy linked to the acoustic scale. The full joint contour shows that consistent (Ω_{m0}, ω_0) constraints arise only when all three probes are mutually aligned. If their preferred Ω_{m0} values differ, joint constraints may shift toward apparently non- Λ CDM values, as demonstrated in Ref. [10]. Fig. 11 (i.e., (H_0, w_0) -plane) illustrates the complementarity between low-z SNe constraints and intermediate-z BAO measurements. SNe tightly constrain ω_0 at low redshift but leave H₀ largely degenerate without an absolute calibration. BAO partially breaks this degeneracy by linking the observed dimensionless distance ratios to the absolute expansion rate. CMB provides an orthogonal constraint based on the sound horizon at recombination. The combined BAO+CMB+SNe contour is therefore significantly smaller than any individual pairwise combination. However, as in the other projections, the full constraining power is realized only when the datasets share a common Ω_{m0} . In the presence of a SNe-BAO tension, the combined (H_0, ω_0) constraints can be substantially distorted.

V. CONCLUSIONS

We have performed a fully controlled and self-consistent null test of the CPL dark-energy parametrization using mock BAO, CMB, and SNe datasets generated from a common Λ CDM cosmology. This design cleanly separates physical information from the geometric and statistical structure of the likelihood, allowing us to clarify how each probe samples the (ω_0, ω_a) parameter space and why partial likelihoods can mimic evolving dark energy even when none is present.

Our analysis shows that individual probes (BAO, CMB, SNe) and most pairwise combinations (BAO+CMB, BAO+SNe, CMB+SNe) produce noticeable displacements in (ω_0, ω_a) and (Ω_{m0}, H_0) relative to the fiducial Λ CDM values. Although two-probe combinations that include supernovae yield (ω_0, ω_a) values close to (-1,0), they still fail to reconstruct the full cosmological parameter set because SNe alone do not determine the absolute distance scale.

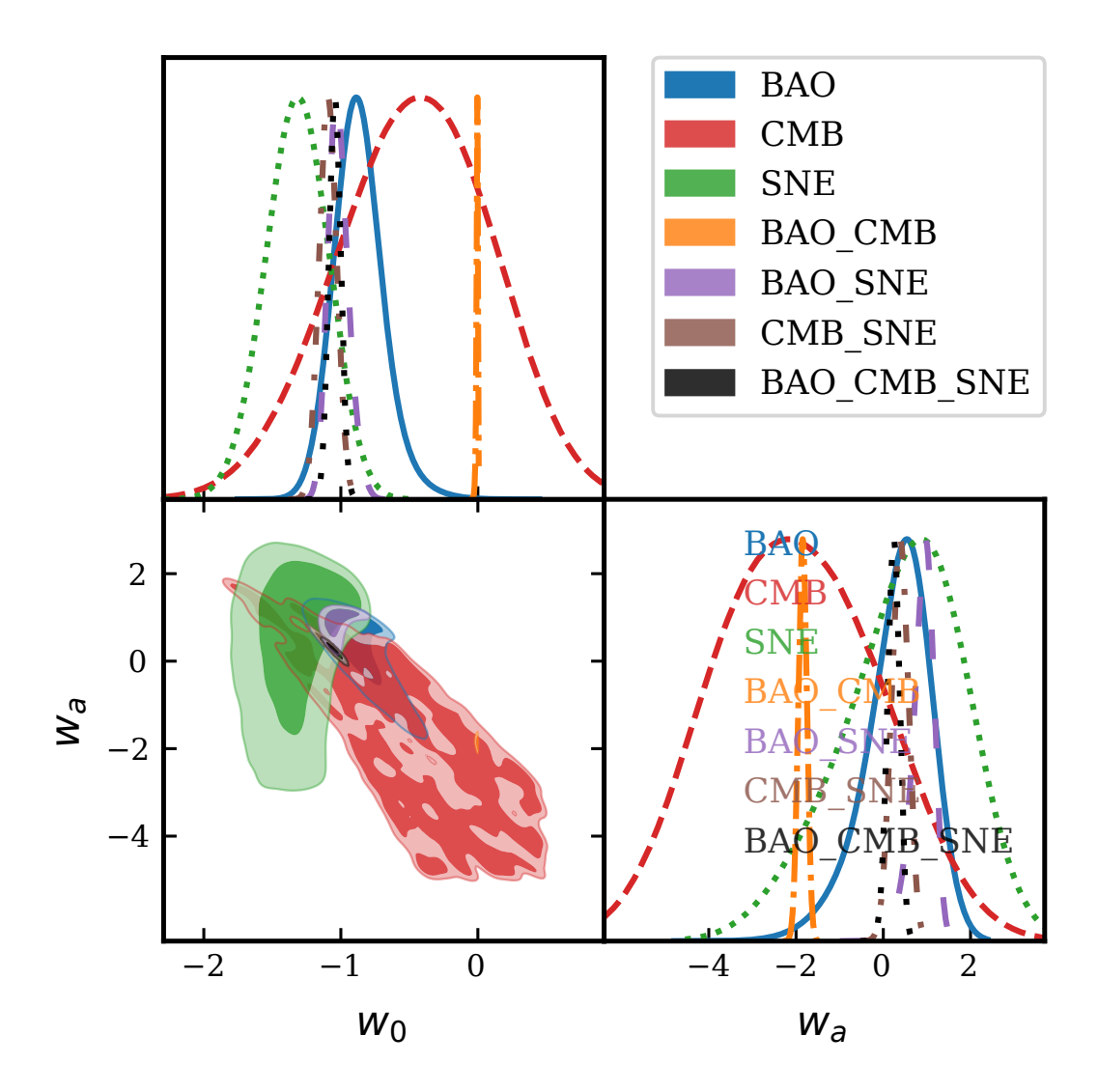


FIG. 8. Constraints on (ω_0, ω_a) from seven probe combinations. Idealized contours demonstrate strong complementarity, although real-data applications may exhibit distortions if Ω_{m0} priors are inconsistent across probes.

Conversely, BAO+CMB combinations retain extended degeneracies in (ω_0, ω_a) due to the absence of low-redshift anchoring. If interpreted at face value, these shifts could be misidentified as signatures of phantom crossing, early dark energy, or rapid late-time transitions.

These apparent signatures are entirely geometric rather than physical. Supernovae constrain a shallow low redshift direction mainly sensitive to ω_0 , BAO constrain an intermediate redshift direction sensitive to combinations of the form $\omega_0 + \beta \omega_a$ with $\beta \simeq 0.5$, and CMB distance priors fix a high redshift direction of the form $\omega_0 + \kappa \omega_a$ with $\kappa \simeq 0.6$ –0.8. Because each probe contains only a different redshift regime, each constrains only a one-dimensional projection of the CPL space. When used in isolation or in partial combinations, the posterior mean naturally shifts along these broad ridges, generating spurious deviations such as $\omega_0 \neq -1$ or $\omega_a \neq 0$ even though the underlying cosmology is exactly Λ CDM. Mathematically, these shifts reflect the geometry of projecting a two-parameter model onto a reduced constraint surface rather than any physical departure from the cosmological constant.

Once the full BAO+CMB+SNe likelihood is used, all these degeneracy directions are simultaneously broken. Because the three one-dimensional ridges intersect uniquely at the fiducial cosmology, the joint posterior collapses to a narrow, well-localized region centered on $(\omega_0, \omega_a) = (-1, 0)$ and correctly recovers (Ω_{m0}, H_0) as well. Thus, the three-probe combination not only yields the smallest statistical uncertainties but also most faithfully reconstructs the true cosmology, demonstrating that the full multi-probe approach is essential for reliable constraints on dynamical dark energy.

These findings have clear implications for current and future surveys, including DESI, Rubin/LSST, Euclid, and

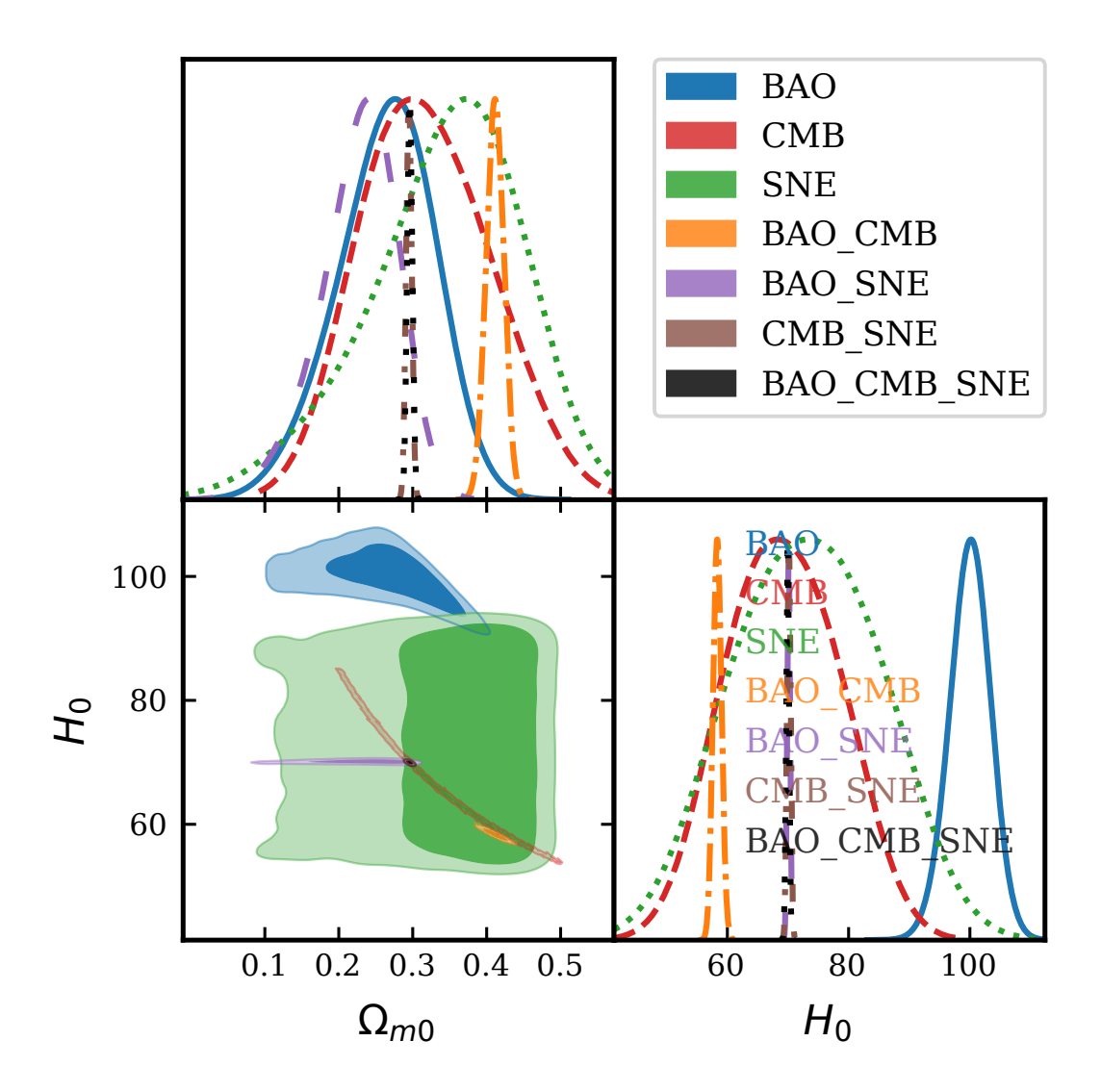


FIG. 9. Constraints in the (Ω_{m0}, H_0) plane. BAO dominates this parameter pair, whereas SNe-only constraints retain a broad degeneracy direction.

future CMB missions. As statistical precision increases, analyses must incorporate the full cross-covariance structure, flexible treatments of r_d and H_0 , and robust internal-tension diagnostics. Any claimed detection of evolving w(z) must remain stable under complete multi-probe combinations and should not rely solely on reduced or compressed likelihoods. Signals of dynamical dark energy that appear only in partial analyses must be considered provisional until they are demonstrated to be consistent across multi-probes.

Overall, this work provides a pedagogically transparent framework for understanding how likelihood geometry, redshift weighting, and probe complementarity shape dark-energy constraints. It also offers a rigorous baseline for interpreting future claims of non- Λ CDM physics and highlights the necessity of unified, consistent multi-probe analyses in the era of high-precision cosmology.

 $^{[1] \} A. \ G. \ Adame \ et \ al. \ [DESI], \ JCAP \ \textbf{02}, \ 021 \ (2025) \ doi: 10.1088/1475-7516/2025/02/021 \ [arXiv:2404.03002 \ [astro-ph.CO]].$

^[3] K. Lodha et al. [DESI], Phys. Rev. D 112, no.8, 083511 (2025) doi:10.1103/w4c6-1r5j [arXiv:2503.14743 [astro-ph.CO]].

 $^{[4] \} M. \ Vincenzi \ et \ al. \ [DES], \ Mon. \ Not. \ Roy. \ Astron. \ Soc. \ {\bf 541}, \ no.3, \ 2585-2593 \ (2025) \ doi:10.1093/mnras/staf943 \ [arXiv:2501.06664 \ [astro-ph.CO]].$

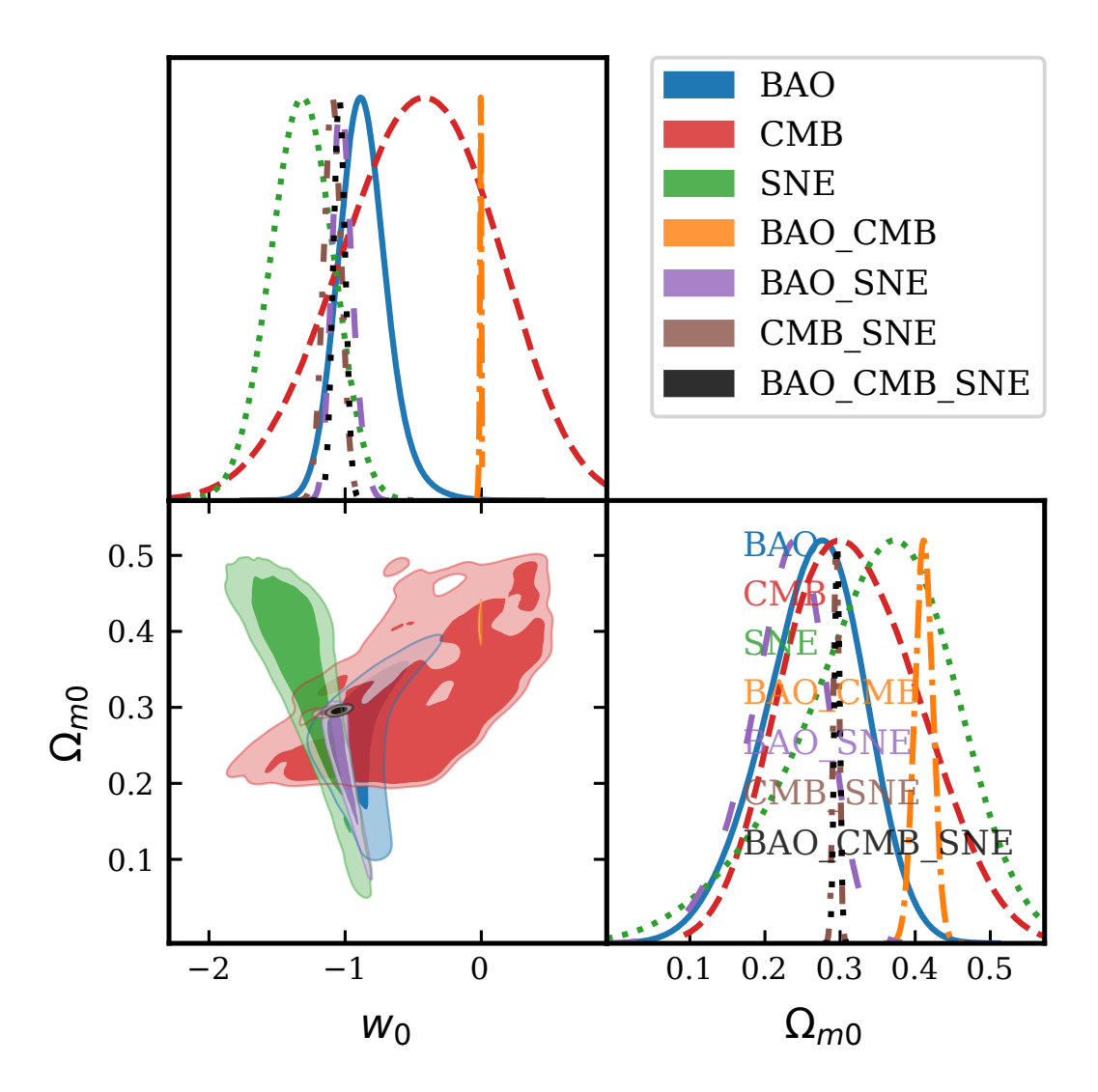


FIG. 10. Joint constraints in (ω_0, Ω_{m0}) for all probe combinations. The full joint analysis minimizes the allowed parameter space, although prior-induced Ω_{m0} tension can shift the combined contours when applied to real data.

- [5] M. Ishak and L. Medina-Varela, [arXiv:2507.22856 [astro-ph.CO]].
- [6] D. Brout, D. Scolnic, B. Popovic, A. G. Riess, J. Zuntz, R. Kessler, A. Carr, T. M. Davis, S. Hinton and D. Jones, et al. Astrophys. J. 938, no.2, 110 (2022) doi:10.3847/1538-4357/ac8e04 [arXiv:2202.04077 [astro-ph.CO]].
- [7] T. L. Smith, M. Lucca, V. Poulin, G. F. Abellan, L. Balkenhol, K. Benabed, S. Galli and R. Murgia, Phys. Rev. D 106, no.4, 043526 (2022) doi:10.1103/PhysRevD.106.043526 [arXiv:2202.09379 [astro-ph.CO]].
- [8] G. Efstathiou, Mon. Not. Roy. Astron. Soc. 538, no.2, 875-882 (2025) doi:10.1093/mnras/staf301 [arXiv:2408.07175 [astro-ph.CO]].
- [9] E. Ó. Colgáin and M. M. Sheikh-Jabbari, [arXiv:2412.12905 [astro-ph.CO]].
- [10] S. Lee, [arXiv:2506.16022 [astro-ph.CO]].
- [11] S. Lee, [arXiv:2506.18230 [astro-ph.CO]].
- [12] D. D. Y. Ong, D. Yallup and W. Handley, [arXiv:2511.10631 [astro-ph.CO]].
- [13] C. Clarkson and R. Maartens, Class. Quant. Grav. 27, 124008 (2010) doi:10.1088/0264-9381/27/12/124008 [arXiv:1005.2165 [astro-ph.CO]].
- [14] A. Heavens, Y. Fantaye, E. Sellentin, H. Eggers, Z. Hosenie, S. Kroon and A. Mootoovaloo, Phys. Rev. Lett. 119, no.10, 101301 (2017) doi:10.1103/PhysRevLett.119.101301 [arXiv:1704.03467 [astro-ph.CO]].
- [15] D. Wang and X. H. Meng, Phys. Rev. D 96, no.10, 103516 (2017) doi:10.1103/PhysRevD.96.103516 [arXiv:1709.01074 [astro-ph.CO]].
- [16] W. Handley and P. Lemos, Phys. Rev. D 100, no.4, 043504 (2019) doi:10.1103/PhysRevD.100.043504 [arXiv:1902.04029 [astro-ph.CO]].

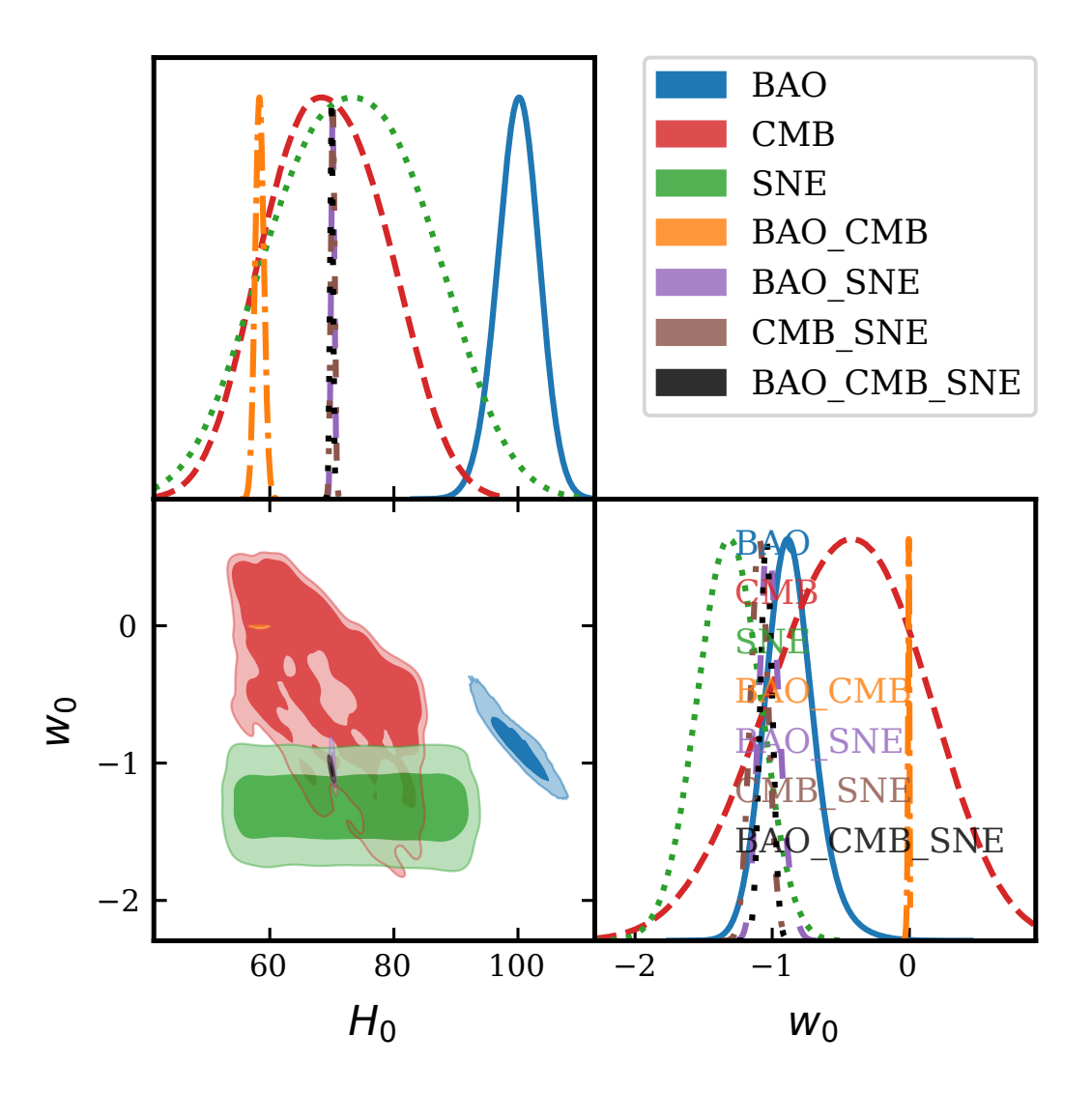


FIG. 11. Constraints in (H_0, ω_0) space. SNe strongly constrain the late-time expansion rate, whereas BAO and CMB constrain the global geometry and normalization.

- [17] G. Efstathiou and S. Gratton, doi:10.21105/astro.1910.00483 [arXiv:1910.00483 [astro-ph.CO]].
- [18] E. Di Valentino, O. Mena, S. Pan, L. Visinelli, W. Yang, A. Melchiorri, D. F. Mota, A. G. Riess and J. Silk, Class. Quant. Grav. 38, no.15, 153001 (2021) doi:10.1088/1361-6382/ac086d [arXiv:2103.01183 [astro-ph.CO]].
- [19] R. Camilleri et al. [DES], Mon. Not. Roy. Astron. Soc. 533, no.3, 2615-2639 (2024) doi:10.1093/mnras/stae1988 [arXiv:2406.05048 [astro-ph.CO]].
- [20] L. Huang, R. G. Cai and S. J. Wang, Sci. China Phys. Mech. Astron. 68, no.10, 100413 (2025) doi:10.1007/s11433-025-2754-5 [arXiv:2502.04212 [astro-ph.CO]].
- [21] W. Giarè, M. Najafi, S. Pan, E. Di Valentino and J. T. Firouzjaee, JCAP 10, 035 (2024) doi:10.1088/1475-7516/2024/10/035 [arXiv:2407.16689 [astro-ph.CO]].
- [22] A. Notari, M. Redi and A. Tesi, JCAP 04, 048 (2025) doi:10.1088/1475-7516/2025/04/048 [arXiv:2411.11685 [astro-ph.CO]].
- [23] A. Albrecht, G. Bernstein, R. Cahn, W. L. Freedman, J. Hewitt, W. Hu, J. Huth, M. Kamionkowski, E. W. Kolb and L. Knox, et al. [arXiv:astro-ph/0609591 [astro-ph]].
- [24] D. Shlivko and P. J. Steinhardt, Phys. Lett. B 855, 138826 (2024) doi:10.1016/j.physletb.2024.138826 [arXiv:2405.03933 [astro-ph.CO]].
- [25] W. Giarè, T. Mahassen, E. Di Valentino and S. Pan, Phys. Dark Univ. 48, 101906 (2025) doi:10.1016/j.dark.2025.101906 [arXiv:2502.10264 [astro-ph.CO]].
- [26] J. Zhang, R. An, S. Liao, W. Luo, Z. Li and B. Wang, Phys. Rev. D 98, no.10, 103530 (2018) doi:10.1103/PhysRevD.98.103530 [arXiv:1811.01519 [astro-ph.CO]].
- [27] N. Jeffrey et al. [DES], Mon. Not. Roy. Astron. Soc. 536, no.2, 1303-1322 (2024) doi:10.1093/mnras/stae2629

- [arXiv:2403.02314 [astro-ph.CO]].
- [28] C. L. Steinhardt, P. Phillips and R. Wojtak, [arXiv:2504.03829 [astro-ph.CO]].
- [29] S. Afroz and S. Mukherjee, [arXiv:2504.16868 [astro-ph.CO]].
- [30] C. Duangchan, A. Valade, N. I. Libeskind and M. Steinmetz, [arXiv:2507.22236 [astro-ph.CO]].
- [31] L. Chen, Q. G. Huang and K. Wang, JCAP 02, 028 (2019) doi:10.1088/1475-7516/2019/02/028 [arXiv:1808.05724 [astro-ph.CO]].
- [32] Z. Zhai, C. G. Park, Y. Wang and B. Ratra, JCAP 07, 009 (2020) doi:10.1088/1475-7516/2020/07/009 [arXiv:1912.04921 [astro-ph.CO]].
- [33] P. Lemos and A. Lewis, Phys. Rev. D 107, no.10, 103505 (2023) doi:10.1103/PhysRevD.107.103505 [arXiv:2302.12911 [astro-ph.CO]].
- [34] M. Chevallier and D. Polarski, Int. J. Mod. Phys. D 10, 213 (2001) doi:10.1142/S0218271801000822 [arXiv:gr-qc/0009008].
- [35] E. V. Linder, Phys. Rev. Lett. **90**, 091301 (2003) doi:10.1103/PhysRevLett.90.091301 [arXiv:astro-ph/0208512].
- [36] D. Huterer and A. Cooray, Phys. Rev. D 71, 023506 (2005) doi:10.1103/PhysRevD.71.023506 [arXiv:astro-ph/0404062 [astro-ph]].
- [37] D. Martin and A. Albrecht, [arXiv:astro-ph/0604401 [astro-ph]].
- [38] D. Scovacricchi, S. A. Bonometto, M. Mezzetti and G. La Vacca, New Astron. 26, 106-111 (2014) doi:10.1016/j.newast.2013.07.005 [arXiv:1211.7315 [astro-ph.CO]].
- [39] X. T. Tang, D. Brout, T. Karwal, C. Chang, V. Miranda and M. Vincenzi, Astrophys. J. Lett. 983, no.1, L27 (2025) doi:10.3847/2041-8213/adc4da [arXiv:2412.04430 [astro-ph.CO]].
- [40] T. M. C. Abbott et al. [DES], [arXiv:2503.06712 [astro-ph.CO]].
- [41] S. F. Chen and M. M. Ivanov, Phys. Rev. D 112, no.8, 083562 (2025) doi:10.1103/3nbk-l5v1 [arXiv:2507.00118 [astro-ph.CO]].
- [42] S. Lee, [arXiv:2507.01380 [astro-ph.CO]].
- [43] M. Tegmark, Astrophys. J. Lett. 480, L87-L90 (1997) doi:10.1086/310631 [arXiv:astro-ph/9611130 [astro-ph]].
- [44] C. B. Morrison and M. D. Schneider, JCAP 11, 009 (2013) doi:10.1088/1475-7516/2013/11/009 [arXiv:1304.7789 [astro-ph.CO]].
- [45] D. Wadekar, M. M. Ivanov and R. Scoccimarro, Phys. Rev. D 102, 123521 (2020) doi:10.1103/PhysRevD.102.123521 [arXiv:2009.00622 [astro-ph.CO]].
- [46] N. Aghanim et al. [Planck], Astron. Astrophys. 641, A6 (2020) [erratum: Astron. Astrophys. 652, C4 (2021)] doi:10.1051/0004-6361/201833910 [arXiv:1807.06209 [astro-ph.CO]].
- [47] A. Lewis, JCAP 08, 025 (2025) doi:10.1088/1475-7516/2025/08/025 [arXiv:1910.13970 [astro-ph.IM]].